

# Statistical Analysis of Northern Australian Coastline Sea Clutter Data

Irina Antipov DSTO-TR-1236

DISTRIBUTION STATEMENT A
Approved for Public Release
Distribution Unlimited

20020514 141

# Statistical Analysis of Northern Australian Coastline Sea Clutter Data

Irina Antipov

Surveillance Systems Division Electronics and Surveillance Research Laboratory

DSTO-TR-1236

#### **ABSTRACT**

This report describes the results of detailed statistical analysis of sea clutter data that were collected during the ESRL 38/97 trial, which was held off the Northern Australian coastline in February 1999. One of the trial's main objectives was to contribute to a database of experimentally collected clutter returns with radar system parameters that are comparable to those used in the Elta EL/M 2022A(V)3 maritime surveillance radar system Anti-Submarine Warfare mode. The validity of the compound K-distribution model has been proven for the collected sea clutter data both for amplitude and correlation properties.

#### RELEASE LIMITATION

Approved for public release

DEPARTMENT OF DEFENCE DEFENCE & TECHNOLOGY ORGANISATION

AQ FO2-08-1583

## Published by

DSTO Electronics and Surveillance Research Laboratory PO Box 1500 Edinburgh South Australia 5111 Australia

Telephone: (08) 8259 5555 Fax: (08) 8259 6567

© Commonwealth of Australia 2001

AR-012-061 November 2001

APPROVED FOR PUBLIC RELEASE

# Statistical Analysis of Northern Australian Coastline Sea Clutter Data

## **Executive Summary**

The Australian Defence Forces (ADF) are currently in the process of acquiring the Israeli built Elta EL/M 2022A(V)3 maritime surveillance radar that will replace the existing APS-115 radar under the Project AIR 5276 – P-3C Update Program. The new radar system will provide the P-3C with a substantial increase in capabilities in both detection and tracking performance and will provide additional target classification capabilities based on high resolution range profiling and Synthetic Aperture Radar imaging. The increase in capabilities is achieved at the cost of a substantial increase in design complexity (compared to the APS-115) including the application of modern digital signal processing techniques, novel radar techniques (such as stepped frequency waveforms) and the implementation of automatic target detection and tracking algorithms.

In order to develop effective and efficient operating procedures, and to understand the strengths and weaknesses of the Elta EL/M 2022A(V)3 maritime surveillance radar system against a variety of targets in Australian environmental conditions, it is necessary to develop a computer model of the system performance. This model must take into account the typical characteristics of the microwave returns from the sea surrounding those targets in the area of operation. The right choice of the sea clutter model among existing models is critical for the correct system detection performance prediction. It must be based on the analysis of sea clutter data that are collected in Australian environmental conditions by a radar system with parameters that are comparable to those used in the Elta EL/M 2022A(V)3 maritime surveillance radar system.

This report describes the results of detailed statistical analysis of sea clutter data that were collected during the ESRL 38/97 trial, which was held off the Northern Australian coastline in February 1999 [1, 2]. One of the main trial objectives was to contribute to a database of experimentally collected clutter returns with radar system parameters that are comparable to those used in the Elta EL/M 2022A(V)3 maritime surveillance radar system Anti-Submarine Warfare mode. The validity of the compound K-distribution model has been proven for the collected sea clutter data both for amplitude and correlation properties.

### **Authors**

## Irina Antipov

Surveillance Systems Division

Dr. Irina Antipov worked as a Research Scientist within the Maritime Sensors Group, Surveillance Systems Division of DSTO from January 1996 to August 2001. From August 2001 she is working as a Senior Research Scientist within the Radio Frequency Countermeasures Group, Electronic Warfare Division of DSTO. Her research interests are in the development of radio frequency countermeasures to airborne maritime radar systems, modelling and evaluation of naval radar systems including: investigating the performance of maritime radar systems, adapting radar systems to operate in a clutter environment, investigating concepts of operation of maritime radar systems.

## **Contents**

1.	INTI	RODUCTION	1			
2.	DAT	A COLLECTION PROCEDURES AND PRE-PROCESSING	2			
	2.1	Timetable	2			
	2.2	Location	2			
	2.3	Airborne Radar	2			
	Sea State Truthing      Sea Clutter Data Collection Procedure      Data Summary					
	2.7	Data Despoking	9			
		2.7.1 Removal of Radar Frequency Interference from Data	9			
		2.7.2 Detection of Spokes in Sampled Return	9			
		2.7.3 Replacement of Spokes in Sampled Return				
3.	STAT	TISTICAL ANALYSIS OF SEA CLUTTER DATA	. 12			
	3.1	Analysis of In-phase and Quadrature Components				
		3.1.1 Analysis of In-phase and Quadrature Components Amplitude				
		Distribution	.15			
		3.1.2 Analysis of Received Sea Clutter Signals Phase Distribution				
	3.2	Sea Clutter Amplitude Probability Density Function Analysis				
		3.2.1 Amplitude Probability Density Function Modelling				
		3.2.2 Moments Analysis	.23			
		3.2.3 Modified Chi-square Test				
		3.2.4 Cumulants Domain Analysis				
	3.3	Compound K-distribution Model	.30			
	3.4	Correlation Analysis				
		3.4.1 Temporal Correlation Properties				
		3.4.1.1 Coherent Temporal Analysis	.35			
		3.4.1.2 Incoherent Temporal Analysis	.38			
		3.4.1.2.1 Speckle Temporal Correlation Properties	.38			
		3.4.1.2.2 Texture Temporal Correlation Properties	.39			
		3.4.1.2.3 Comparison of Model - Based and Nonparametrically Estimated				
		Intensity Temporal Autocorrelation Functions				
		3.4.2 Spatial Correlation Properties	43			
		3.4.2.1 Coherent Spatial Analysis	45			
		3.4.2.2 Incoherent Spatial Analysis	46			
		3.4.2.2.1 Speckle Spatial Correlation Properties	48			
		3.4.2.2.2 Texture Spatial Correlation Properties	49			
		3.4.2.2.3 Comparison of Model - Based and Nonparametrically Estimated				
		Intensity Spatial Autocorrelation Functions	56			
	3.5	Spectral Analysis	56			
		3.5.1 Frequency-Time Analysis	58			
		3.5.2 Averaged Doppler Spectrum Analysis	62			
	3.6	Range-Time-Intensity Plot Analysis	76			

4. SUMMARY80
5. ACKNOWLEDGEMENTS81
6. REFERENCES82
List of tables
Table 1: Main Ingara radar system parameters
Table 10: Ratio of theoretical and observed moments for different estimation methods for an azimuth line with the maximum echo signal amplitude in run22884 data set.
Table 11: Ratio of theoretical and observed moments for different estimation methods for an azimuth line with the maximum echo signal amplitude in run22885 data set.
Table 12: Summary of modified chi-square test on sea clutter for an azimuth line with the maximum echo signal amplitude in experimentally collected data sets
Table 14: Summary of the cumulants domain analysis of the sea clutter amplitude distribution for an azimuth line with the maximum echo signal amplitude in experimentally collected data sets
Table 15: Summary of the cumulants domain analysis of the sea clutter amplitude distribution for an azimuth line with the minimum echo signal amplitude in experimentally collected data sets.
Table 16: Normalised observed moments for the speckle component of sea clutter return from azimuth lines with the maximum echo signal amplitude in analysed data sets
Table 17: Spatial correlation of sea clutter

# **List of Figures**

Figure 1: Map of the trial location showing a 200 n miles radius circle centred on Darwin, NT
Figure 2: Ingara Stare mode parameters and processing used for sea clutter data collection during the ESRL 38/97 trial
Figure 3: Boat "Savage" track
Figure 4: Pictorial view of swell (11 February 1999)
Figure 5: Breaking waves and typical froth wash-over on the back of wave (11 February
1999)
Figure 6: Sea clutter collection geometry (Stare mode)
Figure 7: Flight tracks for stare collection of sea clutter
Figure 8: Spectrum of a range line without RFI present
Figure 9: Spectrum of a range line with strong RFI present
Figure 10: Spectrum of a range line with weak RFI present
Figure 11: Spectrum of a range line with RFI present (note 2 dominant spectral lines). 11
Figure 12: Time history of the clutter+noise mixture amplitude in a range cell for
run22886 data set
Figure 13: Time history of the clutter+noise mixture amplitude in a range cell for
run22884 data set
Figure 14: Time history of the clutter+noise mixture amplitude in a range cell for
run22885 data set
Figure 15: Histograms of I and Q components of the clutter+noise mixture in a range
cell of run22886 data set
Figure 16: Histograms of I and Q components of the clutter+noise mixture in a range
cell of run22884 data set
Figure 17: Histograms of I and Q components of the clutter+noise mixture in a range cell of run22885 data set
Figure 18: Comparison of the empirical PDFs of I and Q components of the
clutter+noise mixture in a range cell of run22886 data set with the corresponding
Gaussian PDFs
Figure 19: Comparison of the empirical PDFs of I and Q components of the
clutter+noise mixture in a range cell of run22884 data set with the corresponding
Gaussian PDFs
Figure 20: Comparison of the empirical PDFs of I and Q components of the
clutter+noise mixture in a range cell of run22885 data set with the corresponding
Gaussian PDFs
Figure 21: Typical phase distributions of sea clutter for run22886 data set
Figure 22: Typical phase distributions of sea clutter for run22884 data set
Figure 23: Typical phase distributions of sea clutter for run22885 data set
Figure 24: Comparison of K-distribution PDFs estimated by different methods for an
azimuth line with the maximum echo signal amplitude in run22886 data set 22 Figure 25: Comparison of K-distribution PDFs estimated by different methods for an
azimuth line with the maximum echo signal amplitude in run22884 data set 22
Figure 26: Comparison of K-distribution PDFs estimated by different methods for an
azimuth line with the maximum echo signal amplitude in run22885 data set 22

Figure 27: Comparison of different estimated PDFs for an azimuth line with the
maximum echo signal amplitude in run22886 data set
Figure 28: Comparison of different estimated PDFs for an azimuth line with the
maximum echo signal amplitude in run22884 data set
Figure 29: Comparison of different estimated PDFs for an azimuth line with the
maximum echo signal amplitude in run22885 data set
Figure 30: Normalised data texture estimate time history for run22886 data set [N=64-
yellow, N=128 - green, N=256 - blue, N=512 - red, N=1028 - black, 2048 - cyan] 32
Figure 31: Normalised data texture estimate time history for run22884 data set [N=64-
yellow, N=128 - green, N=256 - blue, N=512 - red, N=1028 - black, N=2048 - cyan]
32
Figure 32: Normalised data texture estimate time history for run22885 data set [N=64-
yellow, N=128 - green, N=256 - blue, N=512 - red, N=1028 - black, N=2048 - cyan]
Figure 33: Comparison of the empirical PDF of normalised data speckle component in
a range cell of run22886 data set with the corresponding Rayleigh PDF
(normalised mean level)
Figure 34: Comparison of the empirical PDF of normalised data speckle component in
a range cell of run22884 data set with the corresponding Rayleigh PDF
(normalised mean level)
Figure 35: Comparison of the empirical PDF of normalised data speckle component in
a range cell of run22885 data set with the corresponding Rayleigh PDF
(normalised mean level)33
Figure 36: Comparison of the empirical PDF of normalised data texture component in a
range cell of run22886 data set with the corresponding Gamma PDF34
Figure 37: Comparison of the empirical PDF of normalised data texture component in a
range cell of run22884 data set with the corresponding Gamma PDF34
Figure 38: Comparison of the empirical PDF of normalised data texture component in a
range cell of run22885 data set with the corresponding Gamma PDF34
Figure 39: Sea clutter returns temporal correlation function for an azimuth line from
run22886 data set [ TACF  - yellow, Im (TACF) - green, Re (TACF) - red]. Grazing
angle 1.14°, upwind look direction36
Figure 40: Sea clutter returns temporal correlation function for an azimuth line from
run22884 data set [ TACF - yellow, Im (TACF) - green, Re (TACF) - red]. Grazing
angle 2.37° cross-wind look direction
Figure 41: Sea clutter returns temporal correlation function for an azimuth line from
run22885 data set [ TACF  - vellow, Im (TACF) - green, Re (TACF) - red]. Grazing
angle 0.59°, intermediate look direction 135°
Figure 42: Sea clutter returns temporal correlation function for an azimuth line from
run22879 data set [ TACF - yellow, Im (TACF)- green, Re (TACF)- red]. Grazing
angle 1.14°, intermediate look direction 225°
Figure 43: Speckle temporal correlation function for an azimuth line from run22886
data set [Im(TACF)- green, Re(TACF)- red]40
Figure 44: Speckle temporal correlation function for an azimuth line from run22884
data set [Im(TACF)- green, Re(TACF)- red]40
Figure 45: Speckle temporal correlation function for an azimuth line from run22885
data set [Im(TACF)- green, Re(TACF)- red]40

Figure 46: Texture temporal correlation function for run22886 data set [N=64 - yellow
N=128 - green, N=256 - blue, N=512 - red, N=1028 - black, N=2048 - cyan] 41
Figure 47: Texture temporal correlation function for run22884 data set [N=64 - yellow
N=128 - green, N=256 - blue, N=512 - red, N=1028 - black, N=2048 - cyan] 42
Figure 48: Texture temporal correlation function for run22885 data set [N=64 - yellow
N=128 - green, N=256 - blue, N=512 - red, N=1028 - black, N=2048 - cyan] 42
Figure 49: Texture temporal covariance function for run22886 data set [N=64 - yellow
N=128 - green, N=256 - blue, N=512 - red, N=1028 - black, N=2048 - cyan] 42
Figure 50: Texture temporal covariance function for run22884 data set [N=64 - yellow
N=128 - green, N=256 - blue, N=512 - red, N=1028 - black, N=2048 - cyan] 42
Figure 51: Texture temporal covariance function for run22885 data set [N=64 - yellow]
N=128 - green, N=256 - blue, N=512 - red, N=1028 - black, N=2048 - cyan]
Figure 52: Intensity temporal correlation function for an azimuth line from run22886
data set [model-based - green, nonparametrically estimated - red]
Figure 53: Intensity temporal correlation function for an azimuth line from run22884
data set [model-based - green, nonparametrically estimated - red]
Figure 54: Intensity temporal correlation function for an azimuth line from run22885
data set [model-based - green, nonparametrically estimated - red]
Figure 55: Sea clutter returns spatial correlation function for run22886 data set
Figure 55. Sea citater returns spatial correlation function for run22000 data set
[ SACF - yellow, Im (SACF) - green, Re (SACF) - red]. Grazing angle 1.14°,
upwind look direction
Figure 56: Sea clutter returns spatial correlation function for run22884 data set
[ SACF - yellow, Im (SACF) - green, Re (SACF) - red]. Grazing angle 2.37°, cross-
wind look direction
Figure 57: Sea clutter returns spatial correlation function for run22885 data set
[ SACF - yellow, Im (SACF) - green, Re (SACF) - red]. Grazing angle 0.59°,
intermediate look direction 135°
Figure 58: Speckle spatial correlation function for run22886 data set [Im (SACF)- green,
Re (SACF)- red]
Figure 59: Speckle spatial correlation function for run22884 data set [Im (SACF)- green,
Re (SACF)- red]
Figure 60: Speckle spatial correlation function for run22885 data set [Im (SACF)- green,
Re (SACF)- red]
Figure 61: Typical range profile of clutter mean level for run22886 data set
(upwind/upswell). Grazing angle 1.14°51
Figure 62: Typical range profile of clutter mean level for run22884 data set (cross-
wind/cross-swell). Grazing angle 2.37° 51
Figure 63: Typical range profile of clutter mean level for run22885 data set
(intermediate look direction). Grazing angle 0.59°51
Figure 64: Texture spatial correlation function for run22886 data set (upwind/upswell)
Figure 65: Texture spatial correlation function for run22884 data set (cross-wind/cross-
swell)53
Figure 66: Texture spatial correlation function for run22885 data set (intermediate look)
53
Figure 67: Texture spatial covariance function for run22886 data set (upwind/upswell)
54
Figure 68: Texture spatial covariance function for run22884 data set (cross-wind/cross-
swell)

and the second s
Figure 69: Texture spatial covariance function for run22885 data set (intermediate look
direction)
Figure 70: Intensity spatial correlation function for run22886 data set [model-based -
green, nonparametrically estimated - red]
Figure 71: Intensity spatial correlation function for run22884 data set [model-based -
Figure 71: Intensity spatial correlation function for fun
green, nonparametrically estimated - red]
Figure 72: Intensity spatial correlation function for run22885 data set [model-based -
green, nonparametrically estimated - red]
Figure 73: Frequency-time analysis for a single range cell from run22886 data set 61
Figure 74: Frequency-time analysis for a single range cell from run22884 data set 61
Figure 75: Frequency-time analysis for a single range cell from run22885 data set 61
Figure 76: Frequency-time analysis for run22886 data set (log <sub>10</sub> intensity scale)
Figure 77: Frequency-time analysis for run22884 data set (log <sub>10</sub> intensity scale)
Figure //: Frequency-line analysis for run22005 data set (logic intensity scale)
Figure 78: Frequency-time analysis for run22885 data set (log <sub>10</sub> intensity scale)
Figure 79: Sea clutter spectrum for an azimuth line from run22886 data set
Figure 80: Sea clutter spectrum for an azimuth line from run22884 data set
Figure 81: Sea clutter spectrum for an azimuth line from run22885 data set
Figure 82: Averaged sea clutter spectra for run22886 data set
Figure 83: Averaged sea clutter spectra for run22884 data set
Figure 85: Averaged sea clutter spectra for run22885 data set
Figure 84: Averaged sea clutter spectra for funzzooo data set
Figure 85: Range-time-intensity plot for run22886 data set (log <sub>10</sub> intensity scale)
Figure 86: Range-time-intensity plot for run22884 data set (log <sub>10</sub> intensity scale)
Figure 87: Range-time-intensity plot for run22885 data set (log <sub>10</sub> intensity scale)79

### 1. Introduction

The introduction of the Elta EL/M 2022A(V)3 maritime surveillance radar system as the principal sensor within the AP-3C weapon system represents a significant step up in technology and capabilities when compared to the existing AN/APS-115 radar it is replacing. Apart from the considerable improvements in detection performance against small targets, the radar also introduces into the AP-3C new capabilities, including classification modes, which will require re-evaluation of operating procedures and tactics for this platform in order that the new system is deployed effectively.

In order to develop effective and efficient operating procedures, and to understand the strengths and weaknesses of the Elta EL/M 2022A(V)3 maritime surveillance radar system against a variety of targets in Australian environmental conditions, it is necessary to develop a computer model of the system performance. This model must take into account the typical characteristics of the microwave returns from the sea surrounding those targets in the area of operation.

The in-phase and quadrature components of the radar return from the surface of the sea collected by low-resolution radars and at grazing angles greater than about 10° are usually well modelled by independent Gaussian distributions with the same mean and variance. Consequently, the clutter amplitude values for this backscatter are well modelled by a Rayleigh distribution. For higher resolution radars and/or low grazing angles the clutter is often non-Gaussian. The empirical distribution of the observed amplitude returns in these conditions often displays longer tails (higher number of large amplitude values) and larger standard deviation-to-mean ratio than those predicted for a Rayleigh distributed amplitude. The returns are often described as becoming "spiky".

The right choice of the sea clutter model among the most popular existing models (such as Rayleigh, Log-Normal, Weibull and K-distribution) is critical for the correct system performance prediction. It must be based on the analysis of sea clutter data that are collected in Australian environmental conditions by a radar system with parameters that are comparable to those used in the Elta EL/M2022(V)3 maritime surveillance radar system.

This report describes the results of detailed statistical analysis of sea clutter data that were collected during trial ESRL 38/97, which was held off the Northern Australian coastline in February 1999 [1, 2]. One of the trial's main objectives was to contribute to a database of experimentally collected clutter returns with radar system parameters that are comparable to those used in the Elta EL/M 2022A(V)3 maritime surveillance radar system Anti-Submarine Warfare mode. The validity of the compound K-distribution model has been proven for the collected sea clutter data both for amplitude and correlation properties.

# 2. Data Collection Procedures and Pre-processing

#### 2.1 Timetable

The analysed database consists of sea clutter data, which were collected on the 11<sup>th</sup> February 1999 during the maritime radar sea clutter data collection part of trial ESRL 38/97 that took place off the Northern Australian coastline in three days of February 1999 (11, 15 and 16 February) [1, 2].

#### 2.2 Location

The location of trial ESRL 38/97 was limited to the within reasonable flying distance (e.g. radius of 200 n miles) of Darwin, NT, as shown in Figure 1 [1]. The collection of sea clutter returns on 11<sup>th</sup> February was performed approximately 10 nautical miles from the Darwin coastline [2].

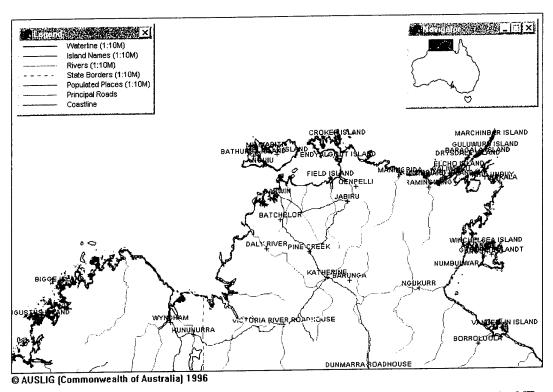


Figure 1: Map of the trial location showing a 200 n miles radius circle centred on Darwin, NT.

#### 2.3 Airborne Radar

The system used to gather the data was the Ingara airborne radar system, developed by Surveillance Systems Division (SSD), in its maritime surveillance configuration with

the vertically polarized elliptical antenna that emulates the antenna used in Elta EL/M 2022A(V)3 radar. It was installed in a Beech King Air 350 aircraft leased by the Australian Army.

The Ingara radar system operates at X-band (9.150-9.650 GHz) with a peak transmitted power of 8 kilowatts and maximum duty cycle of 2%. This system is capable of:

- Transmitting almost any pulsed waveform (up to 80 μs long) repeatedly.
- Centring any pulse anywhere within the 400 MHz bandwidth of the system.
- Analog-to-digital (A/D) sampling with a bandwidth of 100 MHz the in-phase (I) and quadrature (Q) components at 8 bits resolution.

The design of the Stare mode of the Ingara radar that was used for the sea clutter data collection during the trial has been aimed at producing a generic capability that satisfies maritime surveillance mode requirements. In this mode the antenna is kept at a constant look angle with respect to the aircraft flight path while the data is collected. The operation of the Stare mode is shown in Figure 2. The important system parameters common to each sea clutter data collection run are presented in Table 1 [2].

Parameter	Radar specification
Chirp bandwidth	96 MHz
A/D sample rate	100 MHz
Range cell resolution	1.5 m
Pulse width	8 μs
RF centre frequency	9.375 GHz
PRF	500 Hz
Antenna azimuth beamwidth	3.8°
Antenna elevation beamwidth	8°
Polarization	VV

Table 1: Main Ingara radar system parameters.

## 2.4 Sea State Truthing

Parameters pertaining to the sea conditions that are deemed essential to support the analysis are:

- The sea state and/or significant wave height,
- The predominant direction of the waves/swell,
- The wind speed and direction, and
- Changes to the sea or wind conditions.

Due to the lack of any fixed wave buoys in the Northern territory waters, it was originally planned that a directional wave buoy would be hired for the period of the trial and used to record and log the significant wave height, the sea direction and other statistics.

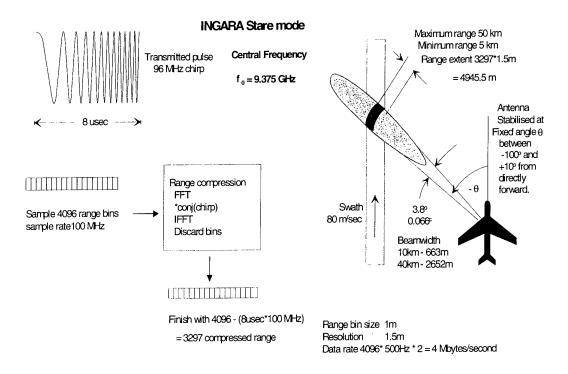


Figure 2: Ingara Stare mode parameters and processing used for sea clutter data collection during trial ESRL 38/97.

However, due to the expense of hiring and deploying this equipment, this idea was dropped in favour of visual observations.

Observations were collected from a chartered vessel – the 27-foot recreational fishing boat "Savage" – and the aircraft. The boat track during the 11-th February trial is shown in Figure 3 [2].

Prior to the data collection flight, the Bureau of Meteorology reported a rainstorm in the area, which was heading North at about 15 knots. This storm cleared the area in time for the aircraft to operate and fly the required patterns.

The sea conditions were dominated by a long wavelength sea swell moving from Northwest, therefore the clutter was modulated by swell. The surface wind, described below, superimposed a structure of spray, capillary waves and froth onto the swell. Froth patches and spray contributed to the backscatter, and the humidity gradient above the surface is expected to affect microwave propagation. Surface wind speed measurements were made with a hand-held anemometer. For the duration of measurements the wind speed was between 10 and 12 knots, from North West: that is, the wind direction was South East 135°, the upwind direction was 315°, all magnetic.

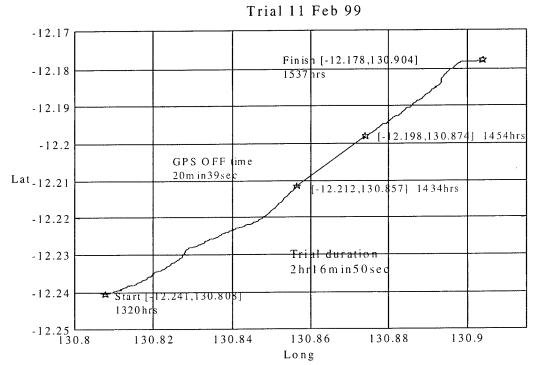


Figure 3: Boat "Savage" track.

Table 2: Sea and wind observation log 11 February 1999 (boat observations).

Parameter	Parameter value	
Sea State Number	2-3	
Wave Height	3-4 m	
Wave Length	15 m	
Wave Period	10-12 sec	
Swell Direction	From the NW	
Wind Direction	From the NW to SE	
Wind Speed	10-12 knots	
Comments	Occasional breaking waves on top of swell Froth patches (2x3m) on back of waves	

Wind waves generated by the local wind could be described as belonging to the moderate sea - the Sea State was roughly estimated to be between 2 and 3. Table 2 summarises the sea conditions recorded.

Table 3 compares the observed values of sea descriptors with those for a fully developed sea [3]. Presented fully developed sea descriptors were calculated for the range of wind speeds that is equal to the observed range of wind speeds. The comparison of the calculated values for fully developed sea descriptors with their

observed values reveals that the data were collected for the conditions of non-equilibrium sea - the data were collected under conditions of changing wind speed before the waves were fully developed. Figures 4 and 5 show photographs of the sea.

Table 3: Comparison of sea descriptors (11 February).

Sea Descriptor	Equation for the Fully Developed Sea Value	Fully Developed Sea Value	Observed Value
Wind Speed	U	5.14 - 6.17 m/sec	5.14 - 6.17m/sec
Wave Period	T = 0.64 U	3.29 - 3.95 sec	10 - 12 sec
Wave Length	$\Lambda = 0.64 \text{ U}^2$	16.91 - 24.36 m	15 m
Root-Mean-Square Height above the Mean Surface Level	$h_{RMS} = 0.005U^2$	0.132 - 0.190 m	1.0 - 1.33 m
Significant Wave Height	$h_{1/3} \cong 3h_{RMS}$	0.396 - 0.571 m	3 – 4 m

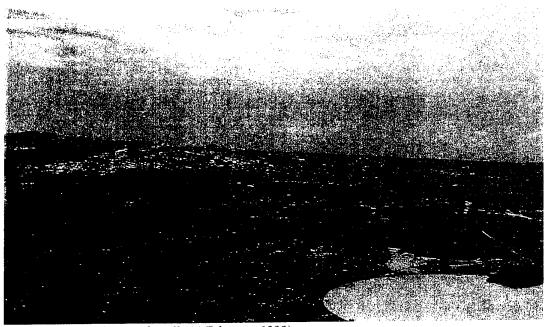


Figure 4: Pictorial view of swell (11 February 1999).

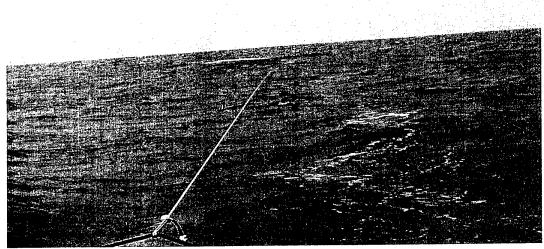


Figure 5: Breaking waves and typical froth wash-over on the back of wave (11 February 1999).

#### 2.5 Sea Clutter Data Collection Procedure

The analysed sea clutter data were collected using the Stare mode with the antenna at 90° relative to the aircraft flight path. The collection procedure results in data being recorded from a strip of the sea surface (Figure 6) [2].

The objective was to collect sea clutter returns at different radar (azimuth) beam angles with respect to the sea swell (wind direction) as this dependence is very important for clarification of the sea clutter model [5, 10, 16, 17].

#### 2.6 Data Summary

The geometry of the data collection runs is presented in Figure 7 - the data were collected from a particular region of the sea from different look angles. The summary of the collected data is shown in Table 4. The parameters in Table 4 were determined as follows:

- 1. Surface range to swath was measured across the Earth surface from directly below the aircraft to the start of the swath.
- 2. Averaged values of surface range to swath and the aircraft altitude above the Earth surface were calculated as these parameters varied pulse-to-pulse due to the deviation of the aircraft from the ideal track. They can be read from the auxiliary data exactly for each pulse if required.
- 3. Antenna pointing relative to the swell angle was based on a swell direction estimate of 135° (i.e. from the North West). By definition 0° is looking straight into swell. The antenna was fixed to point at -90° (i.e. to port side).

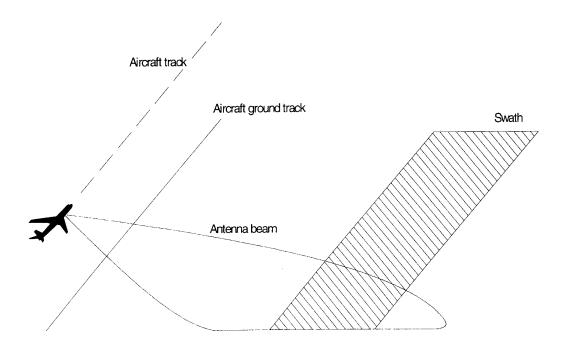


Figure 6: Sea clutter collection geometry (Stare mode).

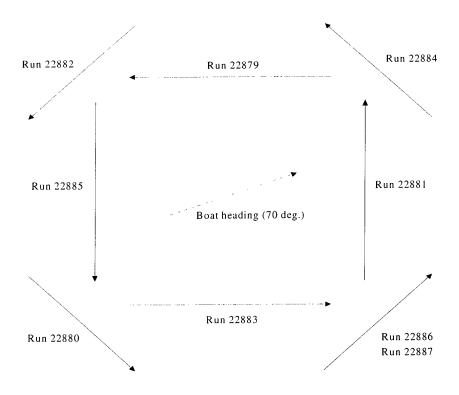


Figure 7: Flight tracks for stare collection of sea clutter

135°

 $0^{\circ}$ 

0°

RUN ID	PRF (Hz)	Total pulses in file	Number of raw and range compressed samples	Surface range to swath (m)	Aircraft altitude (m)	Aircraft heading	Antenna pointing relative to swell
22879	500	122084	4096 / 3297	7928	182	270°	225°
22880	500	96573	4096 / 3297	7928	182	135°	90°
22881	500	108522	4096 / 3297	7928	182	0°	315°
22882	500	117088	4096 / 3297	7928	182	225°	180°
22883	500	94970	4096 / 3297	7928	182	90°	45°
22884	500	117698	4096 / 3297	3928	182	315°	270°
h			<del> </del>				

13928

7928

7928

182

182

182

180°

45°

45°

4096 / 3297

4096 / 3297

4096 / 3297

*Table 4: Parameters specific to each run (Stare mode).* 

106714

97327

#### 2.7 Data Despoking

500

500

500

22885

22886

22887

#### 2.7.1 Removal of Radar Frequency Interference from Data

Data collected in the February '99 trial were partially corrupted by radar frequency interference (RFI) or 'spoking' due mainly to the simultaneous operation of the weather radar of the aircraft and the Ingara radar. Spoking usually manifests itself as a bright streak in range as the interfering RF pulse is received during the time the Ingara radar is sampling. It appears as a sinusoidal signal for the duration of the interference pulse. There are also spokes that are not easily seen in amplitude but become evident in any phase or spectral analysis of a range line. These low level (in amplitude terms) spokes may be due to a bi-static effect of an echo from a true target of a weather radar pulse, which is then received by the Ingara radar. The main problem caused by spoking is that spokes appear like bright target returns on weak target returns that change the statistics of analysing data set. Therefore spoking is an unwanted component of the data set and as such it has to be removed from the data.

#### 2.7.2 Detection of Spokes in Sampled Return

The presence of a spoke in a range line can most robustly be determined by looking at the spectrum (magnitude of the FFT squared) of each range line. The presence of a spoke is characterized by unnaturally strong spectral lines in the spectrum whereas for a range line consisting predominantly of clutter, the spectrum would be a relatively flat, "random" spectrum. There may be more than one spectral line associated with a spoke. This spectrum was thresholded to produce "spoke detections". The threshold was lowered until the range lines being flagged as having spokes had no dominant spectral lines. Figure 8 shows the spectrum of a range line with no spoke.

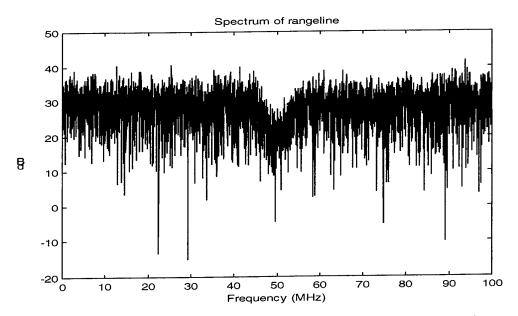


Figure 8: Spectrum of a range line without RFI present (without the shift of zero-frequency component to center of spectrum).

Notice that there are no dominant spectral components.

Figures 9, 10 and 11 show how various cases of spokes in a range line affect the spectrum.

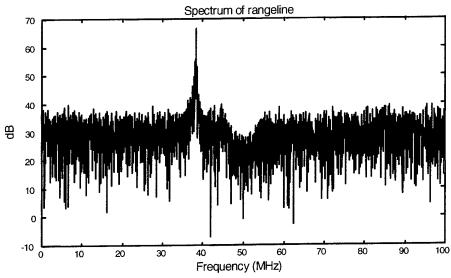


Figure 9: Spectrum of a range line with strong RFI present (without the shift of zero-frequency component to center of spectrum).

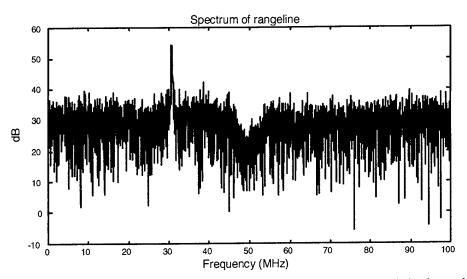


Figure 10: Spectrum of a range line with weak RFI present (without the shift of zero-frequency component to center of spectrum).

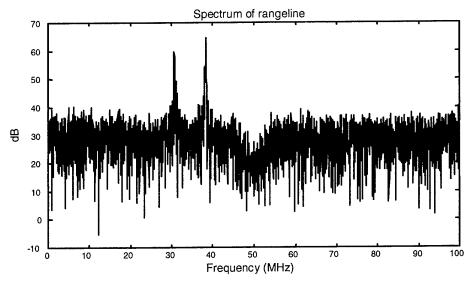


Figure 11: Spectrum of a range line with RFI present (without the shift of zero-frequency component to center of spectrum). Note 2 dominant spectral lines.

### 2.7.3 Replacement of Spokes in Sampled Return

Once a spoke has been detected in a range line, it is desirable to replace that range line with some estimate so that there are no bright streaks appearing in the data. Because the raw sampled data is 8-bit resolution I and Q components, the strong spokes saturate the A/D convertor and no underlying clutter structure can be inferred from the range line. The replacement was done in the range-compressed data (i.e. the detection of spokes was done on the raw sampled data but the replacement was done

on the data produced by the matched filtering). A simple replacement strategy is to replace a spoked range line with some average of the adjacent lines. This is what was done, with each range cell in the range-compressed, spoked range line being replaced by a complex number (I/Q) whose magnitude was the average of the magnitudes of the corresponding range cells in the adjacent lines and whose phase was the averaged phase of these cells. In the case of two consecutive spoked range lines, the replacement lines were linearly interpolated between the adjacent unspoked lines.

# 3. Statistical Analysis of Sea Clutter Data

The wide interest in radar clutter analysis is demonstrated by the large number of research papers published in the literature [4-19, 27-39]. This interest can be explained by the fact that the development of statistical models that properly characterise radar clutter processes are required both for optimum detection algorithm design and for performance prediction.

Radars operating in a maritime environment have a serious limitation imposed on their performance by unwanted sea echoes [3-9, 36]. For low-resolution radars, in which the resolution cell dimensions are much greater than the sea swell wavelength, and for grazing angles greater than about 10°, it is well known that the clutter amplitude is Rayleigh distributed. In modern radar systems operating at low grazing angles and with high-resolution capabilities, the clutter amplitude distribution is observed to develop a longer "tail" and displays a larger standard deviation-to-mean ratio than would be predicted under the Rayleigh distribution [4-7, 21-26]. The sea clutter spikes are processed by the radar detector as targets, giving an increase in false alarm rate. Therefore, representative clutter models are important in evaluating modern radar detection performance, particularly in radars that employ constant false alarm rate processors to adapt the detection threshold to the local clutter and background noise power. For the effective application of theoretical models it is necessary to test their fit with real data using different radar parameters and environmental conditions.

The main aim of this section of the report is to describe the detailed statistical analysis performed on experimental data, which were collected off the Northern Australian coastline with the Ingara radar. The data were collected in order to test the theoretical models that will be used for the detection performance prediction of the Israeli built Elta EL/M2022(V)3 maritime surveillance radar in Australian environmental conditions. In particular, the applicability of the K-distribution for modelling the statistics of low grazing angle sea clutter for a high-resolution radar with the parameters similar to those of the EL/M2022(V)3 radar Anti-Submarine Warfare mode in a sea state 2-3 has been verified.

The detailed description of the statistical analysis of three sets of collected data that represent different flight geometry corresponding to three cases of major interest for the research is presented in the report:

- run22886 data set presents the upswell/upwind flying geometry,
- run22884 data set presents the cross-swell/cross-wind flying geometry, and
- run22885 data set presents the flying geometry with the intermediate look direction compared to the swell direction/wind direction.

Figures 12-14 present time histories of the clutter plus noise mixture amplitude in single range cells from these analysed data sets. As transmitted and received signals had vertical polarization, the sea clutter is not very spiky; however the presence of spikes is evident. The dominant spikes persist for 1-2 seconds. The spikiest response from the sea surface corresponds to the upswell look direction (Figure 12) regardless of the fact that the distance to the analysed range cell in this look direction is twice that of the range cell analysed in the cross-swell look direction (Figure 13). The distance to the range cell analysed in the intermediate look direction (Figure 14) is almost four times longer than to the range cell analysed in the cross-swell/cross-wind look direction. Therefore the clutter-to-noise ratio is much lower in this case and the influence of noise is more evident. Nevertheless all time histories of the clutter plus noise mixture amplitude display a larger standard deviation-to-mean ratio than would be predicted under the Rayleigh distribution.

#### 3.1 Analysis of In-phase and Quadrature Components

This section of the report provides the results of statistical analysis of the amplitude distribution of I and Q components and the phase distribution of experimental data that represent different flying geometry corresponding to the upswell/upwind, cross-swell/cross-wind and intermediate look directions relative to the swell/wind direction.

The amplitude history of received sea clutter signals from a range cell is defined as

$$|Z| = \sqrt{\text{Re}(Z)^2 + \text{Im}(Z)^2}$$
 , (3.1)

where Z is the vector of complex data to be analysed, from a range cell, Re(Z) and Im(Z) are vectors of I and Q component values respectively.

The phase history of received sea clutter signals from a range cell is determined using the corresponding I and Q component values:

$$\Phi = arctg\left(\frac{\operatorname{Im}(Z)}{\operatorname{Re}(Z)}\right),\tag{3.2}$$

where  $\Phi$  is a vector of sea clutter response phases in a range cell.

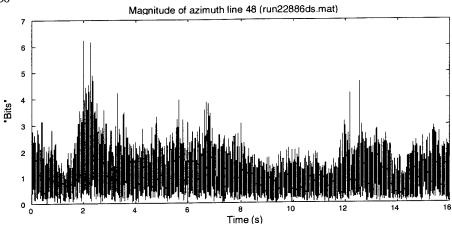


Figure 12: Time history of the clutter+noise mixture amplitude in a range cell for run22886 data set.

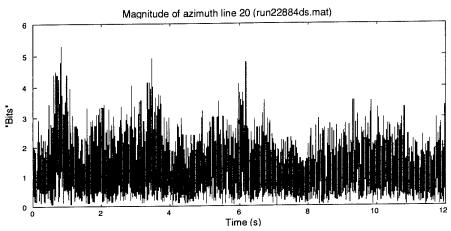


Figure 13: Time history of the clutter+noise mixture amplitude in a range cell for run22884 data set.

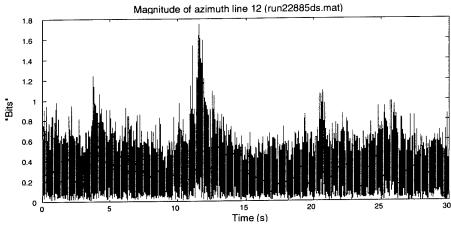


Figure 14: Time history of the clutter+noise mixture amplitude in a range cell for run22885 data set.

Two important results of previous research into coherent properties of the high-resolution sea clutter data collected at low grazing angles [4-6, 11, 36] can be summarised as follows:

- The I and Q components of high-resolution sea clutter data at low grazing angles
  have a non-Gaussian probability density function distribution (PDF) and, hence,
  the amplitude of received sea clutter signals is not Rayleigh distributed, and
- Non-Rayleigh sea clutter phase distribution is practically uniform.

Therefore, we should show that the I and Q components of experimentally collected data have a non-Gaussian PDF and the phase distribution of sea clutter returns is uniform. It would indicate that the Rayleigh model for the sea clutter amplitude PDF does not fit the collected data. Thus, we would confirm the above statements for the sea clutter data collected in Australian environmental conditions by a radar with the parameters similar to those of the EL/M 2022A(V)3 radar Anti-Submarine Warfare mode. The Rayleigh model should then be replaced with other statistical models that are usually used for the analysis of spiky sea clutter [19-26].

# 3.1.1 Analysis of In-phase and Quadrature Components Amplitude Distribution

Figures 15-17 present several examples of histograms of raw I and Q components of sea clutter collected from different range cells of the analysed data sets.

To check whether the I and Q components of experimentally collected data have a Gaussian PDF, histograms of both components were analysed using the approach proposed in [17]. Figures 18-20 show the empirical PDFs of raw I and Q components of the data collected from a single range cell of each analysed data set that are compared with the corresponding Gaussian PDFs having the same mean values and variances. (The mean values are zero as the DC offset of each channel has been estimated from the corresponding entire data set and then removed from the data). It can be seen that the I and Q PDFs deviate from Gaussian in every case, and therefore the clutter amplitude is not Rayleigh distributed in all the analysed experimental data sets.

These results have been confirmed by analysis of skewness  $\gamma_3^Z$  and kurtosis  $\gamma_4^Z$  of empirical PDFs of I and Q components that are defined as follows [17]

$$\left( \gamma_{3}^{Z} \right)_{I,Q} = \frac{E \left\{ \left[ Z_{I,Q} - E \left\{ Z_{I,Q} \right\} \right]^{3} \right\}}{E \left\{ \left[ Z_{I,Q} - E \left\{ Z_{I,Q} \right\} \right]^{2} \right\}^{\frac{3}{2}}} ,$$
 (3.3)

$$(\gamma_4^Z)_{I,Q} = \frac{E\{(Z_{I,Q} - E\{Z_{I,Q}\})^4\}}{E\{(Z_{I,Q} - E\{Z_{I,Q}\})^2\}^2\}} - 3,$$
 (3.4)

#### DSTO-TR-1236

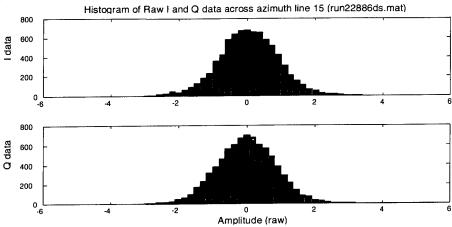


Figure 15: Histograms of I and Q components of the clutter+noise mixture in a range cell of run22886 data set.

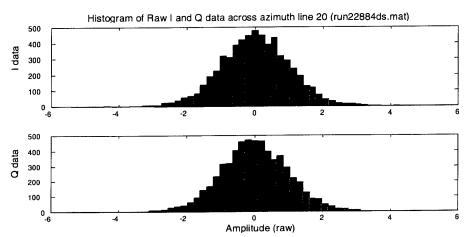


Figure 16: Histograms of I and Q components of the clutter+noise mixture in a range cell of run22884 data set.

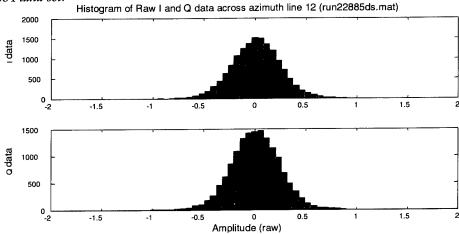


Figure 17: Histograms of I and Q components of the clutter+noise mixture in a range cell of run22885 data set.

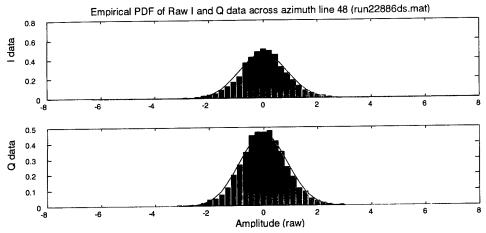


Figure 18: Comparison of the empirical PDFs of I and Q components of the clutter+noise mixture in a range cell of run22886 data set with the corresponding Gaussian PDFs.

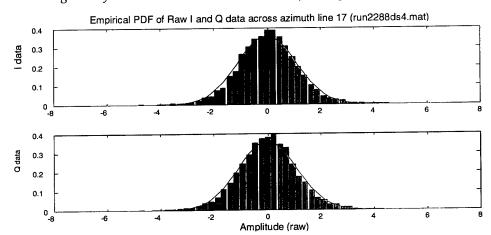


Figure 19: Comparison of the empirical PDFs of I and Q components of the clutter+noise mixture in a range cell of run22884 data set with the corresponding Gaussian PDFs.

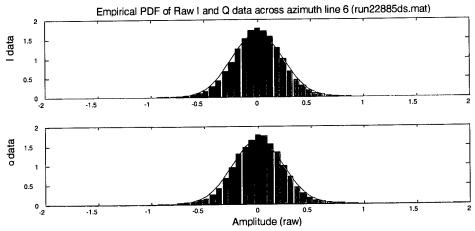


Figure 20: Comparison of the empirical PDFs of I and Q components of the clutter+noise mixture in a range cell of run22885 data set with the corresponding Gaussian PDFs.

where  $E\{a^r\}$  is defined the r -th sample moment,  $Z_{I,Q}$  is the vector of analysing I or Q data from a range cell respectively.

Skewness characterises the degree of asymmetry of a distribution around its mean value. Kurtosis measures the relative peakedness or flatness of a distribution. For a Gaussian PDF, these two parameters are both equal to zero, so they measure deviation of the data from Gaussian. The values of skewness and kurtosis reported in Table 5 for two range cells in every analysed data set show that the asymmetry is not significant; in contrast, peakedness is considerable in all cases.

Run ID	Distribution parameter	First range cell		Second range cell	
		I	Q	I	Q
22886	Skewness	-0.0416	0.0543	-0.0986	-0.0231
	Kurtosis	0.5920	0.5316	1.0994	1.0541
22884	Skewness	-0.0189	0.0201	0.0667	-0.0739
	Kurtosis	0.4336	0.5205	1.0068	0.7667
22885	Skewness	0.0011	-0.0516	-0.0149	-0.0415
	Kurtosis	1.3344	1.0418	1.3396	1.3236

Table 5: Skewness and kurtosis of in-phase (I) and quadrature (Q) component PDFs.

### 3.1.2 Analysis of Received Sea Clutter Signals Phase Distribution

The uniform PDF for phase is defined as

$$p_{\varphi}(\varphi) = \begin{cases} 0 & \text{if} & \varphi < -\pi \\ \frac{1}{2\pi} & \text{if} & -\pi < \varphi < \pi \\ 0 & \text{if} & \varphi > \pi \end{cases}$$
 (3.5)

To check the uniformity of sea clutter phase distributions for the collected data sets, empirical sea clutter phase distributions were calculated for several range cells from each analysed data set.

Figures 21-23 present the resulting typical phase distributions obtained from the considered data sets. The four different colours of each figure correspond to the empirical sea clutter phase distributions for four range cells.

The phase distribution is indeed essentially uniform for each data set.

Thus, the analysed data are characterized by a non-Gaussian nature of the I and Q components and a uniform phase distribution of the sea clutter return and, therefore, they have to be modelled by non-Rayleigh models applied to the spiky sea clutter.

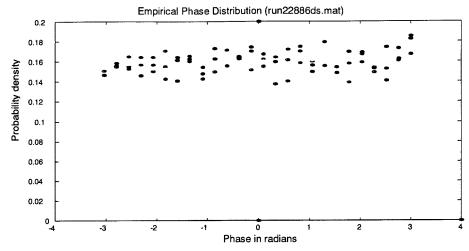


Figure 21: Typical phase distributions of sea clutter for run22886 data set.

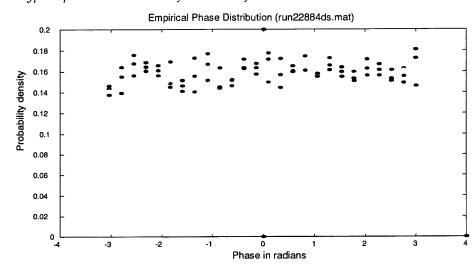


Figure 22: Typical phase distributions of sea clutter for run22884 data set.

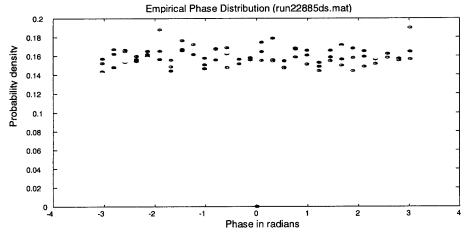


Figure 23: Typical phase distributions of sea clutter for run22885 data set.

## 3.2 Sea Clutter Amplitude Probability Density Function Analysis

Unlike thermal noise or sea clutter returns for a low-resolution radar, most sea clutter returns for a high-resolution radar at low grazing angles are correlated non-Gaussian processes. It was shown in the previous section that the data collected during the ESRL 38/97 trial are characterized by non-Gaussian nature of the I and Q components. Hence these data do not belong to those whose PDF of the amplitude of signals reflected from the sea surface is well modelled by Rayleigh PDF (see Table 6). Therefore, this model should be replaced with other more realistic and self-consistent statistical models that agree with experimental data. Many different distributions have been proposed in the literature to model the amplitude PDF of spiky sea clutter [19-26]. This section of the report briefly presents the most popular spiky sea clutter models, which have been applied to the experimental data collected during the ESRL 38/97 trial, and demonstrates that the K-distribution provides the best results in modelling of the data.

## 3.2.1 Amplitude Probability Density Function Modelling

The most popular models for modelling of spiky sea clutter amplitude PDFs are: Log-Normal [6, 19, 24], Weibull [6, 19, 25] and K-distribution [4-6,19-23, 36]. The expressions for each model cumulative distribution function (CDF), PDF and moments are presented in Table  $6^1$ . In this table, a = |z| is the amplitude of the return signals that is defined for the range  $0 \le a \le \infty$ .

Table 6: Considered models	s for sea clutter amplitude distribution.
----------------------------	---

Model	CDF	PDF	Moments
Rayleigh	$F_{R}(a) = 1 - \exp\left[\left(-\frac{a}{\varpi}\right)^{2}\right]$	$f_R(a) = \frac{2a}{\varpi^2} \exp\left[-\left(\frac{a}{\varpi}\right)^2\right]$	$E_R(a^r) = \varpi^r \Gamma\left(1 + \frac{r}{2}\right)$
Log-Normal	$F_L(a) = \Phi\left(\frac{\ln a - \mu}{\sigma}\right)$	$f_L(a) = \frac{1}{\sqrt{2\pi}\sigma a} \exp\left[-\frac{(\ln a - \mu)^2}{2\sigma^2}\right]$	$E_L(a') = \exp\left(r\mu + \frac{1}{2}r^2\sigma^2\right)$
Weibull	$F_{W}(a) = 1 - \exp\left[-\left(\frac{a}{\varpi}\right)^{\Upsilon}\right]$	$f_{w}(a) = \frac{\gamma}{\varpi} \left( \frac{a}{\varpi} \right)^{y-1} \exp \left[ -\left( \frac{a}{\varpi} \right)^{y} \right]$	
K- distribution	$F_{\kappa}(a) = 1 - \frac{2}{\Gamma(\nu)} \left(\frac{ca}{2}\right)^{\nu} K_{\nu}(ca)$	$f_{K}(a) = \frac{2c}{\Gamma(v)} \left(\frac{ca}{2}\right)^{v} K_{v-1}(ca)$	$E_{K}(a') = \frac{2^{\nu} \Gamma(0.5r+1) \Gamma(0.5r+\nu)}{\Gamma(\nu)c'}$

Definitions:  $\varpi$  is a scale parameter for the Rayleigh and Weibull distributions; r is the order of moment;  $\Gamma(z)$  is the Gamma function;  $\ln(a)$  is Normally distributed with mean  $\mu$  and variance  $\sigma^2$  for Log-Normal distribution;  $\gamma$  is a shape parameter for the Weibull distribution; c is a scale parameter and c0 is a shape parameter for the K-distribution; c1 is the modified Bessel function of the second kind of order c1 and c2 is the error function.

The results of comparing the empirical sea clutter normalised amplitude distribution (each distribution is normalised to its mean [4, 19]) with the considered spiky sea clutter models (Table 6), are summarised in Table 7 and shown in Figures 24 -29 for a range cell with the maximum echo signal amplitude from each analysed data set.

Table 7: Estimates of distribution parameters by different methods for an azimuth line with the
maximum echo signal amplitude in experimentally collected data sets.

RUN ID	Distribution Parameter	Log- Normal	Distribution Parameter	Weibull	K- distrib. (Ragh.)	K- distrib. (Watts)	K- distrib. (FSM)
22886	mean	-0.3450	shape	1.7640	5.4407	2.6785	3.9881
	variance	0.4513	scale	0.9670	4.7049	3.2732	3.9948
22884	mean	-0.3414	shape	1.7771	5.6414	3.4599	4.2957
	variance	0.4489	scale	0.9873	7.6254	3.7202	4.1463
22885	mean	-0.3430	shape	1.7631	5.9253	2.3346	3.9196
	variance	0.4484	scale	0.9664	4.9217	3.0559	3.9602

For the Log-Normal and Weibull distributions the estimates were provided by the maximum likelihood (ML) estimator [19, 24, 25], but because of the difficulty of applying the same estimator to the K-distribution, three well known sub-optimal methods of the K-distribution parameter estimation were used (detailed comparison of these methods is given in [19, 26]):

- Method based on the arithmetic and geometric means estimation, proposed by Raghavan [21], that uses the similarity between the K- and Gamma-distributions,
- Method based on the first and second sample moments estimation (FSM), proposed in [21], and
- Method based on the second and fourth sample moments estimation, proposed by Watts [23].

Analysis of the K-distribution parameter estimation results for the analysed data sets (Figures 24 - 26) shows that:

- The sea clutter of the observed VV-polarized data is not very spiky (that corresponds to the K-distribution shape parameter value v > 2), and
- All methods provide relatively close values of the shape parameter estimate (the shape of the K-distribution PDF becomes less sensitive to the shape parameter value when v > 2 compare to the case of v < 2).

It is well known that the moments based methods are better suited to the estimation of large values of the shape parameter of the K-distribution (v > 2) as the correspondence between the K- and Gamma distributions is weak for such shape parameter values.

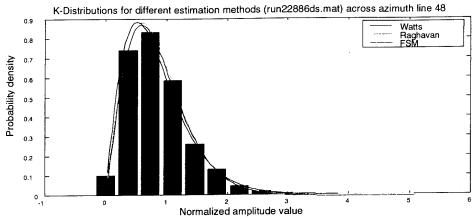


Figure 24: Comparison of K-distribution PDFs estimated by different methods for an azimuth line with the maximum echo signal amplitude in run22886 data set.

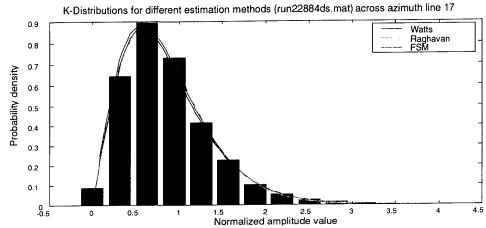


Figure 25: Comparison of K-distribution PDFs estimated by different methods for an azimuth line with the maximum echo signal amplitude in run22884 data set.

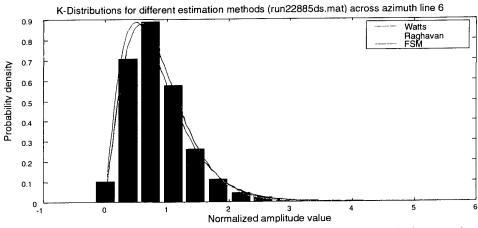


Figure 26: Comparison of K-distribution PDFs estimated by different methods for an azimuth line with the maximum echo signal amplitude in run22885 data set.

Therefore, for the analysed sea clutter data FSM and Watts' methods provide more accurate K-distribution parameter estimates compared to Raghavan's method.

It should be noted that in general thermal noise should not be neglected when analysis of the collected data is performed, as the clutter-to-noise ratio (CNR) may be not very high for some azimuth lines in the analysed data sets (i.e. CNR < 10 dB). In this case the effective value of the K-distribution shape parameter estimated for an analysed azimuth line corresponds to K+thermal noise distribution [23].

Figures 27 - 29 demonstrate fitting of the real data by three most popular models for the spiky sea clutter (Log-Normal, Weibull and K-distribution). It can be seen that for the same data set the K-distribution model (Watts' method) lays between the Log-Normal and the Weibull distribution models in the tail region, as it has been reported by other authors [6, 17]. In order to find, which model provides the best fit to the real data, the moments analysis, modified chi-square test and cumulants analysis were performed on the collected data sets.

#### 3.2.2 Moments Analysis

To investigate the sea clutter behaviour in depth, the comparison of the second, third, fourth, fifth and sixth normalised amplitude moments of the collected data with those for the Rayleigh distribution has been performed. The n-th normalised moment (n = 1, 2, 3, 4, 5, 6) is determined as follows [4, 17]:

$$M_n = \frac{E\{A^n\}}{E^n\{A\}},\tag{3.6}$$

where A = |Z| is the vector of amplitudes of sea clutter return from a range cell.

Table 8 consists of the resulting values of these normalised amplitude moments for the Rayleigh PDF and the collected data from an azimuth line with the maximum echo signal amplitude in each analysed data set. It can be seen that the normalised amplitude moments characterizing the observed data are higher than the corresponding values characterizing the Rayleigh PDF. Therefore, the empirical amplitude distributions for the analysed ESRL 38/97 trial data sets have tails longer than that of the Rayleigh distribution. This is more proof that these data have to be modelled by statistical models, which are usually applied to the spiky sea clutter.

Table 8: Normalised observed moments for the sea clutter return from azimuth lines with the maximum echo signal amplitude in analysed data sets.

Run ID	$M_2$	$M_3$	$M_4$	M 5	$M_{6}$
Rayleigh	1.2732	1.9099	3.2423	6.0793	12.3846
22886	1.3559	2.3438	5.0496	13.4230	43.3790
22884	1.3501	2.2939	4.6992	11.2201	30.3567
22885	1.3573	2.3783	5.2627	14.3838	47.0967

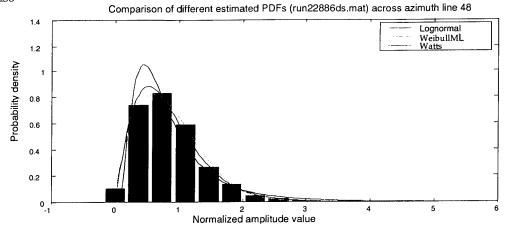


Figure 27: Comparison of different estimated PDFs for an azimuth line with the maximum echo signal amplitude in run22886 data set.

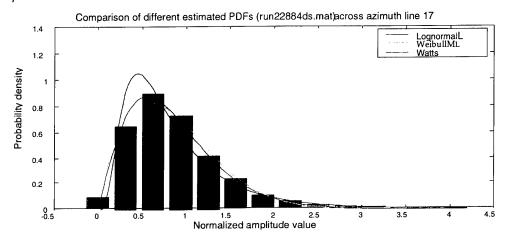


Figure 28: Comparison of different estimated PDFs for an azimuth line with the maximum echo signal amplitude in run22884 data set.

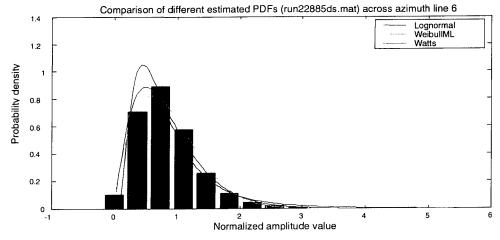


Figure 29: Comparison of different estimated PDFs for an azimuth line with the maximum echo signal amplitude in run22885 data set.

To provide a comparison of the different non-Rayleigh sea clutter models that have been applied to the collected data, the ratio of the theoretical to the observed sample moments for each combination of the parameter estimation and model considered were calculated and compared. Tables 9 - 11 present the results of this analysis for the first to sixth moments ratio for an azimuth line with the maximum echo signal amplitude in each analysed data set.

Table 9: Ratio of theoretical and observed moments for different estimation methods for an azimuth line with the maximum echo signal amplitude in run22886 data set.

Ratio of Moments	Log- Normal	Weibull	K-distribution (Raghavan)	K-distribution (Watts)	K-distribution (FSM)
mt1/mo1	1.0324	1.0024	1.0000	0.9851	1.0000
mt2/mo2	1.2369	0.9951	0.9831	1.0000	0.9996
mt3/mo3	1.8235	0.9413	0.8295	1.0144	0.9762
mt4/mo4	3.4000	0.8262	0.8332	1.0000	0.9101
mt5/mo5	8.0100	0.6597	0.6915	0.9367	0.7948
mt6/mo6	24.5000	0.4771	0.5304	0.8271	0.6468

Table 10: Ratio of theoretical and observed moments for different estimation methods for an azimuth line with the maximum echo signal amplitude in run22884 data set.

Ratio of Moments	Log- Normal	Weibull	K-distribution (Raghavan)	K-distribution (Watts)	K-distribution (FSM)
mt1/mo1	1.0337	1.0023	1.0000	0.9933	1.0000
mt2/mo2	1.2399	0.9959	0.9858	1.0000	0.9995
mt3/mo3	1.8514	0.9534	0.9474	1.0037	0.9851
mt4/mo4	3.6000	0.8741	0.8875	1.0000	0.9553
mt5/mo5	9.4000	0.7711	0.8158	0.9929	0.9166
mt6/mo6	33.8000	0.6604	0.7429	0.9894	0.8774

Table 11: Ratio of theoretical and observed moments for different estimation methods for an azimuth line with the maximum echo signal amplitude in run22885 data set.

Ratio of Moments	Log- Normal	Weibull	K-distribution (Raghavan)	K-distribution (Watts)	K-distribution (FSM)
mt1/mo1	1.0346	1.0023	1.0000	0.9790	1.0000
mt2/mo2	1.2347	0.9940	0.9784	1.0000	0.9997
mt3/mo3	1.7873	0.9280	0.9083	1.0176	0.9650
mt4/mo4	3.2000	0.7932	0.7834	1.0000	0.8782
mt5/mo5	7.3000	0.6163	0.6248	0.9378	0.7483
mt6/mo6	21.7000	0.4401	0.4665	0.8448	0.6033

It can be seen that for all the analysed data sets:

- The results for the Log-Normal distribution model suggest overestimation of the tail length of the experimental data amplitude histogram;
- The lower moments for the Weibull distribution model are in a good agreement with the real data but the higher moments are underestimated indicating a shorter distribution tail length compared to the experimental data amplitude histogram;
- The K-distribution model provides the best fit to the experimental data amplitude histogram compared to Log-Normal and Weibull distribution models;
- The K-distribution model under Raghavan's method provides the most similar results to those for the Weibull distribution model among all considered methods of the K-distribution parameter estimation;
- The K-distribution model under Watts' method has the best higher moments ratio among all the combinations considered;
- The results for the K-distribution model under the FMS method lays roughly between those for the K-distribution model under Raghavan's and Watts' methods for all analysed data sets.

## 3.2.3 Modified Chi-square Test

To verify the results of the experimental amplitude histograms fitting by various models in the tail regions of the PDFs that correspond to the low probability of false alarm (PFA) region, the modified chi-square test was proposed [5, 6]. Boundaries of intervals in this test are determined for each of the statistical models in the amplitude region for which PFA is less than or equal to 0.1, assuming a zero weighting in the amplitude region where PFA is greater than 0.1. Thus, the modified chi-square index is defined as

$$\chi_m^2 = \sum_{k=1}^K \frac{[f_k - N(0.1p_k)]^2}{N(0.1p_k)},$$
(3.7)

where K is the number of intervals into which the low PFA region of the statistical model is divided,  $f_k$  is the observed number of occurrences of a clutter sample having an amplitude within the k-th interval, N is the total number of amplitude samples forming the histogram, and  $N(0.1p_k)$  is the weighted expected number of occurrences in the k-th interval for the statistical model in the low PFA region.

A lower modified chi-squared index  $\chi_m^2$  value indicates a better fit of the model to the data being considered. Tables 12 and 13 summarise the modified chi-square tests on sea clutter for azimuth lines with the maximum and the minimum echo signal amplitudes in the analysed experimentally collected data sets.

Table 12: Summary of modified chi-square test on sea clutter for an azimuth line with the maximum echo signal amplitude in experimentally collected data sets.

RUN ID	Log- Normal	Weibull	K-distribution (Raghavan)	K-distribution (Watts)	K-distribution (FSM)
22886	9533.7	8217.9	6810.1	5346.7	5768.8
22884	7742.9	4962.2	4842.3	4095.2	4307.7
22885	17019	30207	13915	7975	9763

Table 13: Summary of the modified chi-square test on the sea clutter for an azimuth line with the minimum echo signal amplitude in experimentally collected data sets.

RUN ID	Log- Normal	Weibull	K-distribution (Raghavan)	K-distribution (Watts)	K-distribution (FSM)
22886	7491.7	6004.1	6190.2	5732.6	5857.1
22884	5410.4	4607.0	4790.83	4491.4	4557.8
22885	13010	11524	11710	11630	11644

The good fit to the K-distribution is confirmed for all analysed data. The comparison of the modified chi-squared index  $\chi_m^2$  values for all considered models shows that the best results in the important low PFA region can be achieved by applying the K-distribution model to the sea clutter data.

Among the K-distribution parameter estimation methods, the PDF with the parameters using Watts' method gives the best fit to the experimental amplitude histogram in this region.

### 3.2.4 Cumulants Domain Analysis

To perform a deeper analysis of the K+thermal noise model, the theory of cumulants has been applied to the clutter coherent samples, as was suggested in [17].

As it is well known, cumulants of order higher than 2 for a Gaussian process are identically zero. Thus, considering the process

$$z[n] = y[n] + w[n], \tag{3.8}$$

where w[n] is a Gaussian process and y[n] is a non-Gaussian process, independent of w[n], it can be noted that

$$c_{k}^{z}[l_{1},...,l_{k-1}] = c_{k}^{y}[l_{1},...,l_{k-1}] + c_{k}^{w}[l_{1},...,l_{k-1}]$$

$$= c_{k}^{y}[l_{1},...,l_{k-1}] \quad \text{for} \quad k \ge 3$$
(3.9)

Therefore the cumulants of y[n] can be derived from the cumulants of z[n].

As the I and Q components of the thermal noise are zero-mean Gaussian processes, then only non-Gaussian clutter contributes to the third, fourth and fifth order cumulants of the observed data. Since the k-th-order cumulants can be expressed in terms of moments of order  $p \le k$ , sample moments of  $c_k^z[l_1,...,l_{k-1}]$  can be obtained from data estimates of  $m_z^z[l_1]$ ,  $m_3^z[l_1,l_2]$ ,...,  $m_k^z[l_1,...,l_{k-1}]$ . For k=3,4,5 the values of  $c_k^z[l_1,...,l_{k-1}]$  are determined as [17]:

$$\hat{c}_{3}^{I}[l_{1}, l_{2}] = c_{3}^{Q}[l_{1}, l_{2}] = \frac{1}{2N} \sum_{n=0}^{N-1-l_{1}} z_{I}[n] z_{I}[n+l_{1}] z_{I}[n+l_{2}] + z_{Q}[n] z_{Q}[n+l_{1}] z_{Q}[n+l_{2}],$$
(3.10)

where  $0 \le l_2 \le l_1 \le N-1$ .

$$\hat{c}_{4}^{\prime}[l_{1}, l_{2}, l_{3}] = c_{4}^{\varrho}[l_{1}, l_{2}, l_{3}] = \hat{m}_{4}^{\prime}[l_{1}, l_{2}, l_{3}] - \hat{m}_{2}^{\prime}[l_{1}]\hat{m}_{2}^{\prime}[l_{2} - l_{3}] - \hat{m}_{2}^{\prime}[l_{2}]\hat{m}_{2}^{\prime}[l_{3} - l_{1}] - \hat{m}_{2}^{\prime}[l_{3}]\hat{m}_{2}^{\prime}[l_{1} - l_{2}]$$

$$(3.11)$$

$$\hat{c}_{5}^{I}[l_{1}, l_{2}, l_{3}, l_{4}] = c_{5}^{Q}[l_{1}, l_{2}, l_{3}, l_{4}] = \hat{m}_{5}^{I}[l_{1}, l_{2}, l_{3}, l_{4}] - \hat{m}_{3}^{I}[l_{1}, l_{2}]\hat{m}_{2}^{I}[l_{4} - l_{3}] - \hat{m}_{3}^{I}[l_{1}, l_{3}]\hat{m}_{2}^{I}[l_{4} - l_{2}] \\ - \hat{m}_{3}^{I}[l_{2} - l_{1}, l_{3} - l_{1}]\hat{m}_{2}^{I}[l_{4}] - \hat{m}_{3}^{I}[l_{2}, l_{3}]\hat{m}_{2}^{I}[l_{4} - l_{1}] - \hat{m}_{3}^{I}[l_{2} - l_{1}, l_{4} - l_{1}]\hat{m}_{2}^{I}[l_{3}] \\ - \hat{m}_{3}^{I}[l_{3} - l_{1}, l_{4} - l_{1}]\hat{m}_{2}^{I}[l_{2}] - \hat{m}_{3}^{I}[l_{3} - l_{2}, l_{4} - l_{2}]\hat{m}_{2}^{I}[l_{1}] - \hat{m}_{3}^{I}[l_{2}, l_{4}]\hat{m}_{2}^{I}[l_{2} - l_{1}] \\ - \hat{m}_{3}^{I}[l_{2}, l_{4}]\hat{m}_{2}^{I}[l_{3} - l_{1}]$$

$$(3.12)$$

Given N samples of  $z[n] = z_1[n] + z_Q[n]$  (in complex envelope notation), the p-th-order moments (for  $p \le 5$ ) are estimated using

$$\hat{m}^{I}[l_{1},...,l_{p-1}] = \hat{m}_{p}^{Q}[l_{1},...,l_{p-1}] = \frac{1}{2N} \sum_{n=0}^{N-1-l_{1}} \{z_{I}[n]z_{I}[n+l_{1}]...z_{I}[n+p-l_{1}] + z_{Q}[n]z_{Q}[n+l_{1}]...z_{Q}[n+p-l_{1}]\}$$
(3.13)

where  $0 \le l_{p-1} \le ... \le l_2 \le l_1 \le N-1$ .

For the K-distribution coherent model, all the cumulants of odd order calculated at the origin are equal to zero, while for the second and forth cumulants the following relations hold true:

$$c_2'[0] = c_2^{\varrho}[0] = \frac{2v}{c^2},$$
 (3.14)

$$c_4^{\prime}[0,0,0] = c_4^{\varrho}[0,0,0] = \frac{16\nu}{c_4^{\prime}},$$
 (3.15)

where c is the scale parameter and v is the shape parameter of the K-distribution PDF and  $\hat{c}_2'[0] = \hat{c}_2^Q[0] = m_2'[0] = m_2^Q[0]$ .

To compare the values of  $\hat{c}_3'[0,0]$ ,  $\hat{c}_4'[0,0,0]$  and  $\hat{c}_5'[0,0,0,0]$  with theoretical cumulants of the coherent K-distribution model, all cumulants have been normalised with respect to the corresponding second order cumulant as follows [17]:

$$\mu_{k} = \frac{c_{k}'[0,0,...,0]}{\left(c_{k}'[0]\right)^{k/2}} = \frac{c_{k}^{\varrho}[0,0,...,0]}{\left(c_{k}^{\varrho}[0]\right)^{k/2}}$$
(3.16)

Tables 14 and 15 present a summary of the cumulants domain analysis for azimuth lines with the maximum and the minimum echo signal amplitudes in the analysed experimentally collected data sets.

Table 14: Summary of the cumulants domain analysis of the sea clutter amplitude distribution for an azimuth line with the maximum echo signal amplitude in experimentally collected data sets.

RUN ID	Theoretical $\hat{\mu}_2$	Real $\hat{\mu}_5$	Theoretical $\hat{\mu}_{4}$	Real $\hat{\mu}_{_4}$	Theoretical $\hat{\mu}_5$	Real $\hat{\mu}_{\scriptscriptstyle 5}$
22886	0	0.0360	1.4934	1.1651	0	1.6255
22884	0	-0.0077	1.1561	0.8996	0	0.3396
22885	0	0.0269	1.7733	1.3344	0	-0.9380

Table 15: Summary of the cumulants domain analysis of the sea clutter amplitude distribution for an azimuth line with the minimum echo signal amplitude in experimentally collected data sets.

RUN ID	Theoretical	Real $\hat{\mu}_{5}$	Theoretical	Real $\hat{\mu}_{\scriptscriptstyle 4}$	Theoretical	Real $\hat{\mu}_5$
	$\hat{\mu}_{\scriptscriptstyle 3}$	, ,	$\hat{\mu}_{\scriptscriptstyle 4}$	·	$\hat{\mu}_{\scriptscriptstyle 5}$	
22886	0	-0.0253	0.2376	0.2266	0	0.0336
22884	0	0.0571	0.2571	0.1997	0	-0.0190
22885	0	-0.0537	0.2581	0.1907	0	0.1236

Analysis of the results of comparing the values of  $\hat{c}_3'[0,0]$ ,  $\hat{c}_4'[0,0,0]$  and  $\hat{c}_5'[0,0,0,0]$  with theoretical cumulants of the coherent K-distribution model shows that:

• The values of the real cumulants that have been estimated as in equations (3.10)-(3.12) are close to the theoretical values that have been obtained from the estimates of *c* and *v* by Watts' method (this method was chosen as it gives a better fit to the

experimental amplitude histogram in the low PFA region than the others methods of estimation of the K-distribution parameters);

- As expected for the K-distribution model,  $\hat{\mu}_3 \approx 0$  and  $\hat{\mu}_5 \approx 0$ ;
- The deviation of  $\hat{\mu}_4$  from the K-distribution model is small for all analysed data.

Therefore, a good fit of the collected data with the K-distribution model is confirmed.

# 3.3 Compound K-distribution Model

In its compound form, the K-distribution model is decomposed into two components [4-6, 17, 19-23, 36]. According to this model the overall disturbance |z| can be presented as the product of a local Rayleigh component x (referred to as speckle) by a root-Gamma component y (referred to as texture) that modulates the power level relative to the underlying sea swell:

$$|z| = \sqrt{y}x\tag{3.17}$$

The PDF of these two components are defined respectively:

• For the texture *y*:

$$p_z(y) = \frac{1}{\Gamma(v)} \left(\frac{c^2}{2}\right)^v y^{v-1} \exp(-\frac{c^2}{2}y),$$
 (3.18)

where c is the scale parameter (such that  $c^2 = \pi \frac{v}{E(y)}$ , where E(y) is the average power of the clutter) and v is the shape parameter.

• For the speckle *x* that has a mean level determined by the first component *y*:

$$p_x(x/y) = \frac{\pi x}{2y} \exp\left(-\frac{\pi x^2}{4y}\right)$$
 (3.19)

The considered components x and y show two different decorrelation times. The speckle has a short temporal decorrelation period on the order of tens of milliseconds, and can be decorrelated from pulse to pulse by frequency agility. The texture has a long temporal decorrelation period on the order of a few seconds and it is not affected by frequency agility.

Therefore, in a short time period the mean level can be assumed constant and the speckle component can be isolated by considering short time sequences. On the other hand, the texture component can be isolated by averaging the modulus-squared data over a window of short time duration, to remove the speckle effect [4, 17].

To estimate the duration of these short time sequences, the time history of the texture was estimated from a moving window of the collected data, assuming that the thermal noise is negligible [17]:

$$|\hat{y}_i| = \frac{1}{2N} \sum_{n=1}^{N} |z_i[n]|^2 \tag{3.20}$$

with different values of the window length N from 64 to 2048 samples. Here  $\{z_i[n]\}_{n=1}^N$  are the coherent clutter samples from the i – th block).

Figures 30-32 present the results of the texture time history estimation for a range cell with the maximum echo signal amplitude in each analysed data set.

It can be seen that 64- and 128-point estimates of z exhibit high variance around the mean value, due to the speckle variation. In contrast, the 1024- and 2048-point curves are more regular, but they do not follow the mean trend. It means that the durations of 1024 and 2048 samples exceed the invariability time.

Analysis has indicated the underlying texture component to be strongly correlated over a period of about 0.5 sec. Therefore, to isolate the speckle component, sequences of 256 sweeps (0.5 sec. at 500 Hz PRF) of clutter data were analysed and amplitude histograms were calculated. The results of comparing the speckle component empirical PDF with the corresponding Rayleigh PDF in a single range cell of each analysed data set are presented in Table 16 and shown in Figures 33-35.

Table 16: Normalised observed moments for the speckle component of sea clutter return from azimuth lines with the maximum echo signal amplitude in analysed data sets.

Run ID	$M_2$	$M_3$	$M_4$	$M_{5}$	$M_{6}$
Rayleigh	1.2732	1.9099	3.2423	6.0793	12.3846
22886	1.2773	1.9378	3.3489	6.3952	13.1819
22884	1.2694	1.9046	3.2543	6.1624	12.6504
22885	1.2800	1.9595	3.4331	6.6669	13.7575

The results indicate that the speckle component is indeed Rayleigh distributed.

In order to isolate the texture component, averaging of modulus-squared data over a window of 128 ms (64 sweeps) was implemented to remove the speckle effect. This procedure, described by equation (3.25), was applied to several range cells in each analysed data set. The amplitude histograms of the resulting disturbance for a single range cell from each data set are plotted in Figures 36-38. As a comparison, every Figure also shows the Gamma theoretical PDF having the same first- and second-order moments. The fit with the data is good, as expected for the K-distribution model.

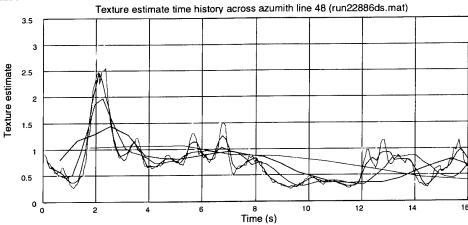


Figure 30: Normalised data texture estimate time history for run22886 data set [N=64 - yellow, N=128 - green, N=256 - blue, N=512 - red, N=1028 - black, 2048 - cyan].

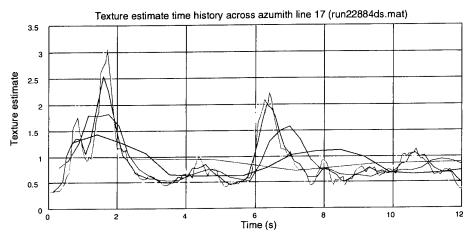


Figure 31: Normalised data texture estimate time history for run22884 data set [N=64 - yellow, N=128 - green, N=256 - blue, N=512 - red, N=1028 - black, N=2048 - cyan].

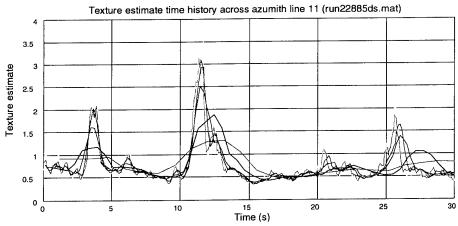


Figure 32: Normalised data texture estimate time history for run22885 data set [N=64 - yellow, N=128 - green, N=256 - blue, N=512 - red, N=1028 - black, N=2048 - cyan].

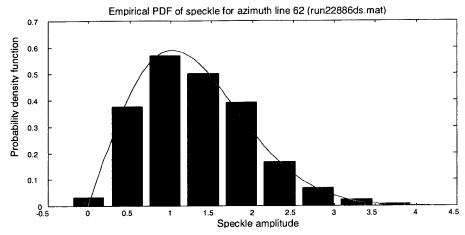


Figure 33: Comparison of the empirical PDF of normalised data speckle component in a range cell of run22886 data set with the corresponding Rayleigh PDF (normalised mean level).

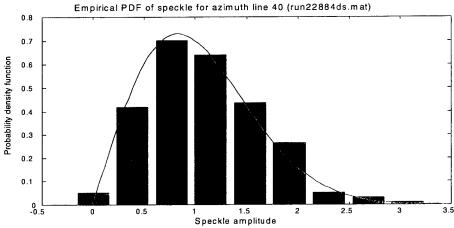


Figure 34: Comparison of the empirical PDF of normalised data speckle component in a range cell of run22884 data set with the corresponding Rayleigh PDF (normalised mean level).

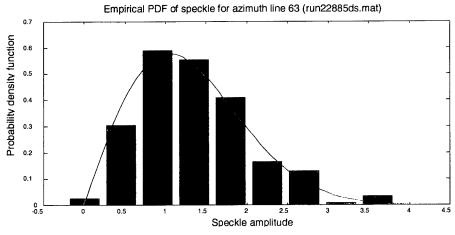


Figure 35: Comparison of the empirical PDF of normalised data speckle component in a range cell of run22885 data set with the corresponding Rayleigh PDF (normalised mean level).

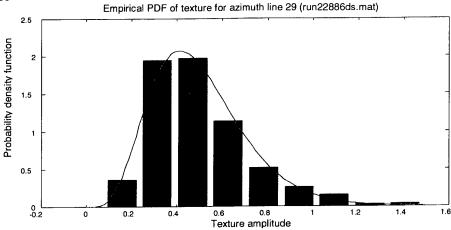


Figure 36: Comparison of the empirical PDF of normalised data texture component in a range cell of run22886 data set with the corresponding Gamma PDF.

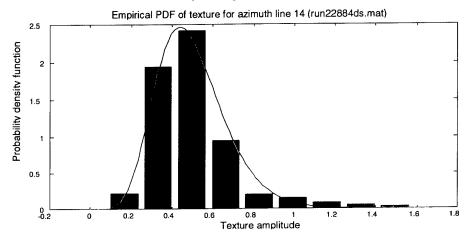


Figure 37: Comparison of the empirical PDF of normalised data texture component in a range cell of run22884 data set with the corresponding Gamma PDF.

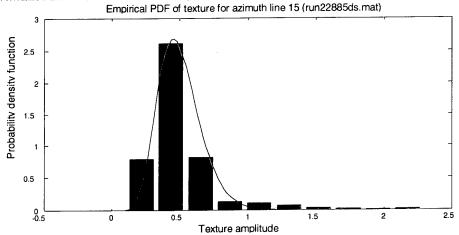


Figure 38: Comparison of the empirical PDF of normalised data texture component in a range cell of run22885 data set with the corresponding Gamma PDF.

### 3.4 Correlation Analysis

As an accurate prediction of the radar detection performance is usually more dependent on the accurate modelling of temporal and spatial correlation features than on the choice of amplitude distribution [22, 23, 36], it is important to analyse clutter correlation properties.

### 3.4.1 Temporal Correlation Properties

In this section of the report the results of analysis of the temporal correlation properties of sea clutter are presented for a single range cell in each analysed data set. For other cells the results are very similar.

#### 3.4.1.1 Coherent Temporal Analysis

The temporal autocorrelation function (ACF) of the overall disturbance z (3.17) that consists of two components ((3.18) and (3.19)) with different decorrelation times is the product of the ACFs of these two components [17]:

$$R_{z}[m] = E\{z[n]z^{*}[n+m]\} = R_{\sqrt{y}}[m]R_{x}[m] = 2R_{\sqrt{y}}[m](R_{x_{i}}[m] + jR_{x_{i}x_{Qi}}[m])$$
(3.21)

where  $x_I[n]$  and  $x_Q[n]$  are Gaussian-distributed I and Q components of the speckle.

Therefore, the decorrelation time of the coherent signal is equal to that of the faster component. In order to demonstrate this fact, the temporal ACF of the overall disturbance z was estimated for a single range cell in each analysed data set by using M consecutive bursts of N = 256 complex samples:

$$\hat{R}_{z}[m] = \frac{1}{NM} \sum_{i=1}^{M} \sum_{n=0}^{N-m-1} z_{i}[n] z_{i}^{*}[n+m] = 2(\hat{R}_{z_{I}}[m] + j\hat{R}_{z_{I}z_{Q}}[m])$$
(3.22)

where  $z_I[n]$  and  $z_Q[n]$  are the I and Q components and z[n] is the complex envelope of the observed signal.

Figures 39-42 present these estimated normalised temporal ACFs of sea clutter returns for single azimuth lines (range cells) from several analysed experimentally collected data sets. It can be seen that the correlation time of the coherent disturbance is about 6-10 ms in every range cell, which corresponds to the usual value of correlation time of the speckle component of the sea clutter disturbance [29, 17]. It is also evident that there is a non-negligible cross-correlation between I and Q components of the sea clutter return due to a small Doppler shift [5, 6, 17].

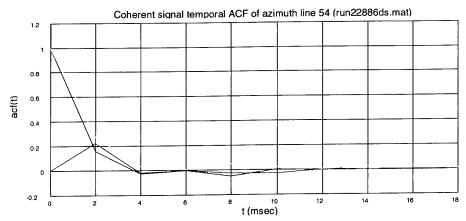


Figure 39: Sea clutter returns temporal correlation function for an azimuth line from run22886 data set [|TACF|- yellow, Im (TACF) - green, Re (TACF) - red]. Grazing angle 1.14°, upwind look direction.

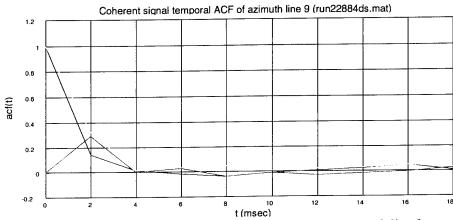


Figure 40: Sea clutter returns temporal correlation function for an azimuth line from run22884 data set [|TACF| - yellow, Im (TACF) - green, Re (TACF) - red]. Grazing angle 2.37°, crosswind look direction.

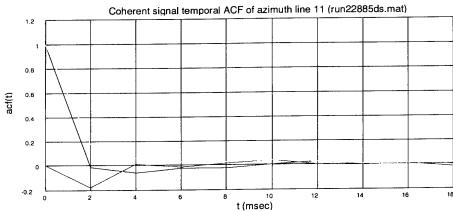


Figure 41: Sea clutter returns temporal correlation function for an azimuth line from run22885 data set [|TACF| - yellow, Im (TACF) - green, Re (TACF) - red]. Grazing angle 0.59°, intermediate look direction 135°.

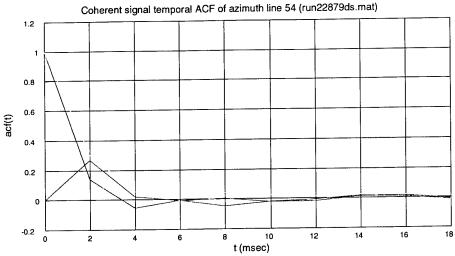


Figure 42: Sea clutter returns temporal correlation function for an azimuth line from run22879 data set [\TACF\-\ yellow, Im (TACF\-\ green, Re (TACF\-\ red]. Grazing angle 1.14°, intermediate look direction 225°.

Detailed analysis of Figures 39-42 shows that coherence properties of low grazing angle sea clutter, which are characterized by the temporal ACF of coherent sea clutter return, are strongly grazing angle and wind direction dependent.

The general results of this analysis are in quantative agreement with the results reported in [29]:

- The short decorrelation time at the initial decay of  $|\hat{R}_z[m]|$  of the order of 10 ms or less is observed;
- The increase of decorrelation time with increasing grazing angle is evident;
- The intermediate look direction temporal ACF of coherent sea clutter return is wider than the upwind look direction ACF for the same grazing angle.

Different scattering mechanisms can be a major cause for the complex nature of the temporal ACF of coherent sea clutter return. For VV polarized coherent sea clutter signals, the mechanisms, which contribute to microwave scattering from ocean waves may include the following [29-31]:

- Scattering from free Bragg waves, characterized by a Gaussian distribution in scatterer speeds, at all angles relative to the wind and at all grazing angles;
- Scattering from fast to intermediate-speed, short-lifetime bound-waves (i.e. short relative to the lifetime of free Bragg waves) at upwind look directions at all grazing angles and/or scattering from facets of shorter gravity waves of different wavelength (and thus with a spread in values of phase speed) at upwind look directions at all grazing angles and
- Multipath scattering at all angles relative to the wind and at all grazing angles.

#### 3.4.1.2 Incoherent Temporal Analysis

To estimate the temporal correlation of the two clutter components separately, it is necessary to analyse the incoherent signal, i.e. the squared amplitude of the coherent signal [17]:

$$I[n] = |\hat{z}[n]|^2 = y[n] \left( x_I^2[n] + x_O^2[n] \right)$$
(3.23)

The temporal ACF of this incoherent signal is determined by

$$R_{I}[m] = R_{v}[m] \left( 2E \left\{ x_{I}^{2}[n]x_{I}^{2}[n+m] \right\} + E \left\{ x_{I}^{2}[n]x_{O}^{2}[n+m] \right\} + E \left\{ x_{I}^{2}[n+m]x_{O}^{2}[n] \right\} \right)$$
(3.24)

If  $x_I[n]$  and  $x_Q[n]$  are jointly Gaussian processes with unit variance and zero mean then the incoherent signal ACF is given by

$$R_{I}[m] = 4R_{y}[m] + 2R_{y}[m]R_{X_{I}}^{2}[m] + 2R_{y}[m]R_{X_{I}X_{O}}^{2}[m]$$
(3.25)

It is evident that the first temporal part of the overall correlation is dominated by the fast component (short-term). At this time interval the long-term correlation can be considered constant (i.e.  $R_y[m] \cong R_y[0]$ ). After a few seconds, the correlation is dominated by the long-term component, because  $R_{X_x}^2[m] \cong R_{X_xX_x}^2[m] \cong 0$ , that is

$$R_{I}[m] \cong 4R_{V}[m] \tag{3.26}$$

If the amplitude of the disturbance can be modelled by a K-distribution then the temporal ACF of the intensity is given by equation (3.25). Therefore, further proof of the validity of the K-distribution model can be obtained by comparing the nonparametrically estimated temporal ACF of the intensity with the temporal ACF parametrically estimated according to equation (3.25) [17].

#### 3.4.1.2.1 Speckle Temporal Correlation Properties

According to Figures 36-39, texture can be considered constant over short time intervals, and the speckle temporal ACF can be estimated by using coherent signal samples from such short intervals. Data bursts of N = 256 samples (0.5 sec) have been considered and the following estimators with M data block have been used to estimate the I and Q speckle components autocorrelation and cross-correlation functions [17]:

$$\hat{R}_{X_{I}}[m] = \frac{1}{M} \sum_{i=1}^{M} \left[ \frac{1}{\hat{y}_{i} 2N} \operatorname{Re} \left\{ \sum_{n=0}^{N-1-m} z_{i}[n] z_{i}^{*}[n+m] \right\} \right]$$
(3.27)

$$\hat{R}_{X_{I}X_{Q}}[m] = \frac{1}{M} \sum_{i=1}^{M} \left[ \frac{1}{\hat{y}_{i} 2N} \operatorname{Im} \left\{ \sum_{n=0}^{N-1-m} z_{i}[n] z_{i}^{*}[n+m] \right\} \right]$$
(3.28)

For each sample set the texture value y has been estimated from the same data using equation (3.20) with N = 256. The resulting speckle components normalised auto- and cross-correlation functions for a single range cell from analysed data sets are presented in Figures 43-45. It can be seen that these functions are in complete agreement with those plotted in Figures 39-41.

#### 3.4.1.2.2 Texture Temporal Correlation Properties

To estimate the texture temporal ACF, estimates of the texture values in *I* data blocks, which have been obtained from equation (3.20), have been used [17]:

$$\hat{R}_{y}[Nl] = \frac{1}{I} \sum_{i=1}^{I-l} \hat{y}_{i} \hat{y}_{i+l}$$
 (3.29)

Note that averaging of N samples to obtain the estimates  $\hat{y}_i$  gives the estimation of  $R_y[m]$  for every N steps (during this time interval the texture is considered to be completely correlated).

The results for a different number of steps N that have been obtained for a single range cell from each analysed data set are presented in Figures 46-48. It can be seen that the normalised texture ACFs corresponding to 64-, 128-, and 256- point estimates of  $\hat{y}_i$  have very similar values to each other.

In contrast, the normalised texture ACFs corresponding to 1024- and 2048-point estimates of  $\hat{y}_i$  exhibit quite different shape. This means that the durations of 1024 and 2048 samples exceed the invariability time.

Figures 49-51 present the texture normalised temporal covariance functions of a single range cell from each analysed data set. They illustrate periodic variations of the mean clutter level with the look direction angle relative to the wind/swell direction change that were observed during the data collection. The autocovariance function is determined as

$$\hat{C}_{y}[Nl] = \frac{1}{I} \sum_{i=1}^{I-l} (\hat{y}_{i} - \overline{y})(\hat{y}_{i+l} - \overline{y}) = \hat{R}_{y}[Nl] - \overline{y}^{2}$$
(3.30)

where  $\bar{y}$  is the texture mean value given by

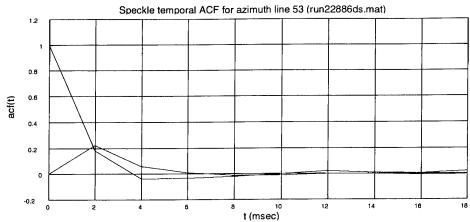


Figure 43: Speckle temporal correlation function for an azimuth line from run22886 data set [Im(TACF)- green, Re(TACF)- red].

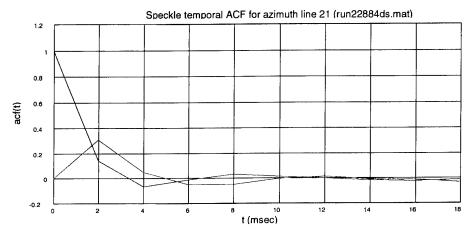


Figure 44: Speckle temporal correlation function for an azimuth line from run22884 data set [Im(TACF)- green, Re(TACF)- red].

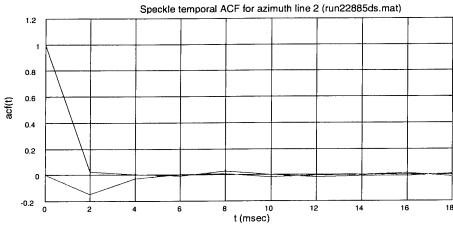


Figure 45: Speckle temporal correlation function for an azimuth line from run22885 data set [Im(TACF)- green, Re(TACF)- red].

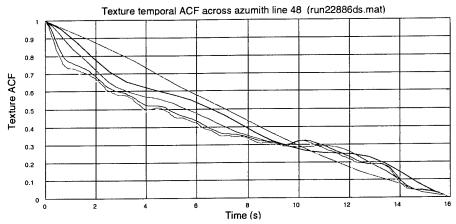


Figure 46: Texture temporal correlation function for run22886 data set [N=64 - yellow, N=128 - green, N=256 - blue, N=512 - red, N=1028 - black, N=2048 - cyan].

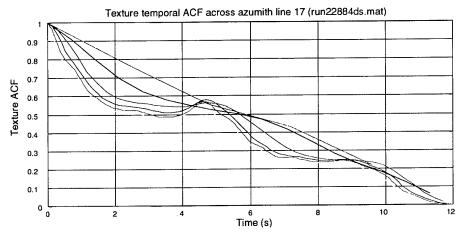


Figure 47: Texture temporal correlation function for run22884 data set [N=64 - yellow, N=128 - green, N=256 - blue, N=512 - red, N=1028 - black, N=2048 - cyan].

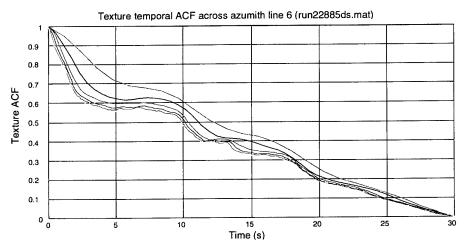


Figure 48: Texture temporal correlation function for run22885 data set [N=64 - yellow, N=128 - green, N=256 - blue, N=512 - red, N=1028 - black, N=2048 - cyan].

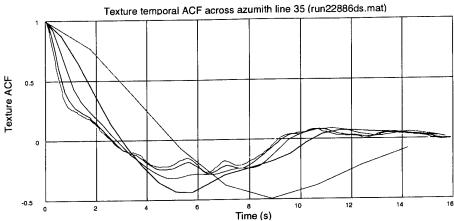


Figure 49: Texture temporal covariance function for run22886 data set [N=64 - yellow, N=128 - green, N=256 - blue, N=512 - red, N=1028 - black, N=2048 - cyan].

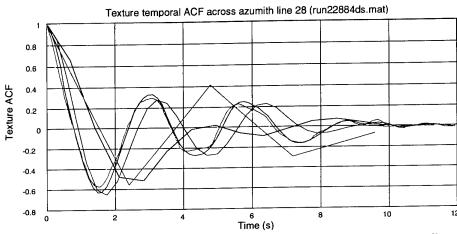


Figure 50: Texture temporal covariance function for run22884 data set [N=64 - yellow, N=128 - green, N=256 - blue, N=512 - red, N=1028 - black, N=2048 - cyan].

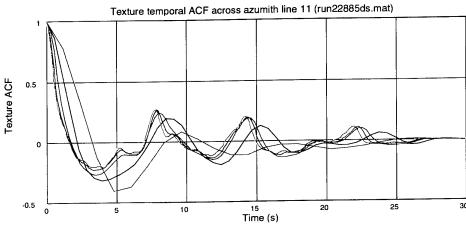


Figure 51: Texture temporal covariance function for run22885 data set [N=64 - yellow, N=128 - green, N=256 - blue, N=512 - red, N=1028 - black, N=2048 - cyan].

$$\overline{y} = \frac{1}{I} \sum_{i=1}^{I} \hat{y}_i \tag{3.31}$$

The longest texture temporal correlation with a period of about 11 sec corresponds to the upwind/upwind look direction (run22886) presented in Figure 49. The wide azimuthal beamwidth tends to filter out waves travelling perpendicular to the radar line of sight via the interference of the returns from multiple independent scattering centers associated with the train of waves falling within the radar footprint. The correlation period of 11 sec is in complete agreement with the observed swell period (Table 2). The periodic variation of the mean clutter level due to a heavy sea swell is evident.

The texture temporal correlation period of about 3 sec corresponds to the cross-swell/cross-wind look direction (run22884) presented in Figure 50. Across the swell, only structure larger than the radar cross-range resolution is resolved in time as the swell moves through the beam.

The temporal correlation period of about 7 sec corresponds to the intermediate look direction (run22885) presented in Figure 51. The relatively wide cross-range footprint of the radar in this case included a mixture of crests and troughs.

3.4.1.2.3 Comparison of Model - Based and Nonparametrically Estimated Intensity Temporal Autocorrelation Functions

Figures 52-54 present the results of comparing the clutter intensity normalised temporal ACF obtained using the compound K-distribution model that is described by equations (3.25) – (3.29) with the overall normalised temporal ACF nonparametrically estimated from a single range cell data z[n] for each analysed data set.

These normalised temporal ACFs are presented for two time scales: the ACFs relative to the first 18 ms are enlarged at the top of Figures 52-54.

It can be seen that the model-based and nonparametrically estimated normalised temporal ACFs of the sea clutter intensity are very similar to each other for each analysed data set. The peak due to speckle correlation is evident.

### 3.4.2 Spatial Correlation Properties

In this section of the report the results of analysis of the spatial correlation properties of sea clutter are presented for each analysed data set.

The spatial correlation of sea clutter is defined as the cross-correlation between the signals returned from two separate patches of the sea in the radial dimension. The time interval separating the measurement of these two signals is assumed to be so small that there is negligible time decorrelation.

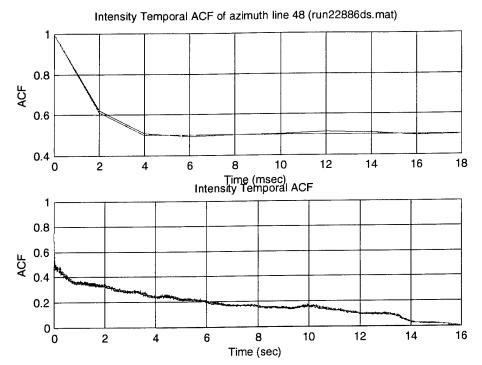


Figure 52: Intensity temporal correlation function for an azimuth line from run22886 data set [model-based - green, nonparametrically estimated - red].

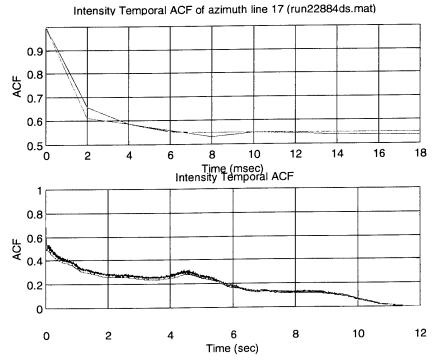


Figure 53: Intensity temporal correlation function for an azimuth line from run22884 data set [model-based - green, nonparametrically estimated - red].

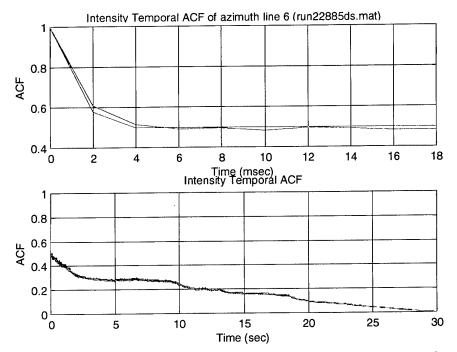


Figure 54: Intensity temporal correlation function for an azimuth line from run22885 data set [model-based - green, nonparametrically estimated - red].

Spatial correlation of sea clutter reflected signals is a well known phenomenon [6, 11, 20, 36, 38, 42], caused by the relation of the sea clutter modulating process to the surface profile of the sea. While microwave signals are primarily scattered by capillary waves of the sea (speckle), the undulating structure of the sea gravity waves causes variations of the mean power scattered from a given patch (modulating process), which are mechanistically explained in terms of bunching of contributing scatterers and local tilting of the sea surface slope. Therefore, it is reasonable to assume that the degree of correlation of the modulating process between resolution cells depends on the spatial correlation of the sea surface, and that this process has a decorrelation distance of the same order of magnitude as the decorrelation distance of the sea.

It is also clear, that in well-developed swell conditions, a periodic component will be present in the spatial ACF of the modulating process. Concerning the correlation properties of the speckle, it is necessary to note that for a given realisation of the large scale structure, the small scale features at two separated patches are usually uncorrelated. Therefore, the speckle is assumed to be entirely decorrelated from one range cell to the next.

#### 3.4.2.1 Coherent Spatial Analysis

The spatial ACF of the overall disturbance z (3.17) that consists of two components ((3.18) and (3.19)) with different range correlation length is the product of the ACFs of these two components:

$$\hat{S}_{z}[l] = E\{z[k]z^{*}[k+l]\} = \hat{S}_{\sqrt{y}}[l]S_{x}[l] = 2\hat{S}_{\sqrt{y}}[l](\hat{S}_{x_{l}}[l] + j\hat{S}_{x_{l}x_{Ql}}[l])$$
(3.32)

where  $x_I[k]$  and  $x_Q[k]$  are Gaussian-distributed I and Q components of the speckle in the k-th range cell.

Therefore, the range correlation length of the coherent signal is equal to that of the faster changing range component. In order to demonstrate this fact, the spatial ACF of the overall disturbance z was estimated for a single time correlation period of the underlying mean clutter level in each analysed data set. This was done by using L = 256 consecutive range lines of  $K = K_{cells}$  complex samples (where  $K_{cells}$  is the number of range cells in one range line):

$$\hat{S}_{z}[l] = \frac{1}{KL} \sum_{n=1}^{L} \sum_{k=0}^{K-l-1} z_{n}[k] z_{n}^{*}[k+l] = 2 \left( \hat{S}_{z_{l}}[l] + j \hat{S}_{z_{l} z_{Q}}[l] \right)$$
(3.33)

where  $z_I[k]$  and  $z_Q[k]$  are the I and Q components and z[k] is the complex envelope of the observed signal from k-th range cell.

Figures 55-57 present these estimated normalised spatial ACFs of the sea clutter returns for the analysed experimentally collected data sets. It can be seen that the range correlation length of the coherent disturbance is less than the radar range resolution. (Note that the original data were sampled at intervals smaller than the radar resolution). It corresponds to the spatial correlation properties of the speckle component of the sea clutter disturbance, which is uncorrelated in range. It is also evident that there is no cross-correlation between I and Q components of the sea clutter return.

Therefore I and Q components of the overall coherent disturbance are spatially independent as are I and Q components of the speckle.

#### 3.4.2.2 Incoherent Spatial Analysis

Using the same approach as for analysis of the temporal correlation properties of two components of sea clutter returns, separate estimation of the spatial correlation of these two components has been achieved by analysis of the incoherent signal, i.e. the squared amplitude of the coherent signal:

$$I[k] = |\hat{z}[k]|^2 = y[k] \left( x_I^2[k] + x_Q^2[k] \right)$$
(3.34)

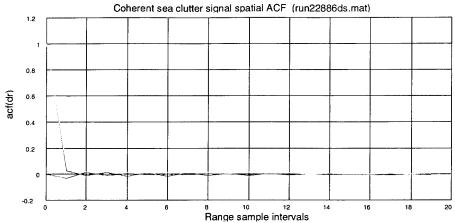


Figure 55: Sea clutter returns spatial correlation function for run22886 data set [|SACF|-yellow, Im (SACF) - green, Re (SACF) - red]. Grazing angle 1.14°, upwind look direction.

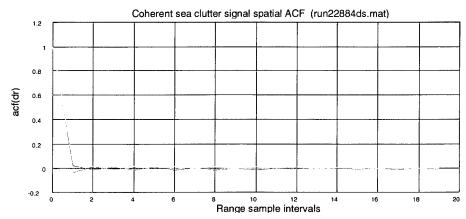


Figure 56: Sea clutter returns spatial correlation function for run22884 data set [|SACF|-yellow, Im (SACF) - green, Re (SACF) - red]. Grazing angle 2.37°, cross-wind look direction.

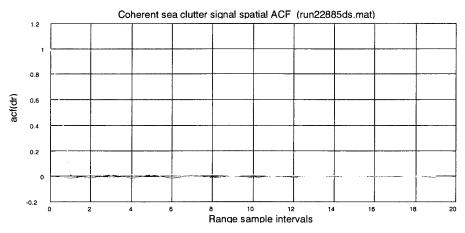


Figure 57: Sea clutter returns spatial correlation function for run22885 data set [|SACF|-yellow, Im (SACF) - green, Re (SACF) - red]. Grazing angle 0.59°, intermediate look direction 135°.

Then the spatial ACF of this incoherent signal is determined by

$$S_{I}[l] = S_{v}[l] \left( 2E \left\{ x_{I}^{2}[k] x_{I}^{2}[k+l] \right\} + E \left\{ x_{I}^{2}[k] x_{Q}^{2}[k+l] \right\} + E \left\{ x_{I}^{2}[k+l] x_{Q}^{2}[k] \right\} \right)$$
(3.35)

If  $x_I[k]$  and  $x_Q[k]$  are jointly Gaussian processes with unit variance and zero mean then the incoherent signal spatial ACF is given by

$$S_{I}[m] = 4S_{y}[m] + 2S_{y}[m]S_{X_{I}}^{2}[m] + 2S_{y}[m]S_{X_{I}X_{Q}}^{2}[m]$$
(3.36)

It is evident that the first part of the overall spatial correlation is dominated by the fast changing range component (short-term). This component is uncorrelated from one range cell to another.

After a single range sample interval, the range correlation is dominated by the long-term component, because  $S_{X_I}^2[m] \cong S_{X_IX_O}^2[m] \cong 0$ , that is

$$S_I[m] \cong 4S_v[m] \tag{3.37}$$

If the amplitude of the disturbance can be modelled by a K-distribution then the spatial ACF of the intensity is given by equation (3.36). Therefore, further proof of the validity of the K-distribution model can be obtained by comparing the nonparametrically estimated spatial ACF of the intensity with the ACF parametrically estimated according to equation (3.36) as it was done for the temporal ACF of the sea clutter intensity.

### 3.4.2.2.1 Speckle Spatial Correlation Properties

As was shown by the analysis of Figures 30-32, texture in a single range cell can be considered constant over short time intervals. The spatial ACF of the speckle component can be estimated using coherent signal samples from consecutive range cells in a number of range lines during such a short interval. Data bursts of  $K = K_{cells}$  spatial samples have been considered and following estimators with L= 256 data block have been used to estimate the I and Q speckle components spatial autocorrelation and cross-correlation functions:

$$\hat{S}_{X_{I}}[l] = \frac{1}{L} \sum_{n=1}^{L} \left[ \frac{1}{2K} \operatorname{Re} \left\{ \sum_{k=0}^{K-1-l} \frac{z_{n}[k]}{\sqrt{\hat{y}_{n}[k]}} \frac{z_{n}^{*}[k+l]}{\sqrt{\hat{y}_{n}[k+l]}} \right\} \right]$$
(3.38)

$$\hat{S}_{X_{I}X_{Q}}[l] = \frac{1}{L} \sum_{n=1}^{L} \left[ \frac{1}{2K} \operatorname{Im} \left\{ \sum_{k=0}^{K-1-l} \frac{z_{n}[k]}{\sqrt{\hat{y}_{n}[k]}} \frac{z_{n}^{*}[k+l]}{\sqrt{\hat{y}_{n}[k+l]}} \right\} \right]$$
(3.39)

For each range cell the texture value y has been estimated from the same data using equation (3.20) with N = 256.

The resulting speckle components normalised spatial auto- and cross-correlation functions for a single range cell from analysed data sets are presented in Figures 58-60. It can be seen that these functions are in complete agreement with those plotted in Figures 55-57.

### 3.4.2.2.2 Texture Spatial Correlation Properties

To estimate the texture ACF, the approach proposed in [40] was used. Each point in range was averaged by integrating successive temporally decorrelated returns from the same range in order to remove the speckle component of the clutter and yield J profiles of the mean clutter level  $\left|\sqrt{\hat{y}_j[k]}\right|$ , k=1,..., K, j=1,..., J. The integration period was chosen to be short compared with the correlation period of the texture (N=256 during this time interval the texture was considered to be completely temporally correlated):

$$\left| \sqrt{\hat{y}_{j}[k]} \right| = \frac{1}{N_{uncor}} \sum_{n=1}^{N_{uncor}} \left| z_{j,k}[n] \right| \tag{3.40}$$

where  $N_{uncor} = \left(\frac{N}{N_{decor} + 1}\right)$  is the number of temporally uncorrelated samples in the

integration period; N is the total number of samples in the integration period;  $N_{decor}$  is the temporal correlation length of the texture, expressed in radar temporal samples, which is equal to 0 if the samples are temporally uncorrelated; and  $z_{j,k}[n]$  is the n-th complex temporally independent clutter sample from k-th range cell in j-th profile.

Figures 61-63 present typical plots of these range profiles of the mean clutter level for the analysed data sets.

The data in Figure 61 was obtained looking upswell/upwind with a grazing angle of 1.14° and at a range of 9.2 km. The range profile shows a strong periodicity with range, which reflects the long wavelength sea swell that was observed at the time. The wind-generated waves on the top of swell have a period of about 15 m that is in agreement with observation data presented in Table 2.

The data in Figure 62 was collected under the same sea conditions but with a grazing angle of 2.37°, a range of 4.4 km and looking cross-swell/cross-wind. This data exhibits

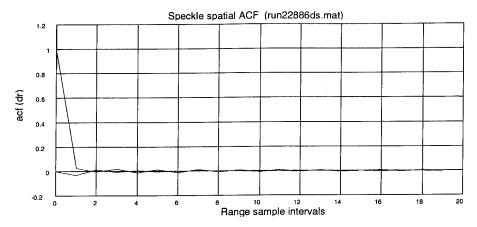


Figure 58: Speckle spatial correlation function for run22886 data set [Im (SACF)- green, Re (SACF)- red].

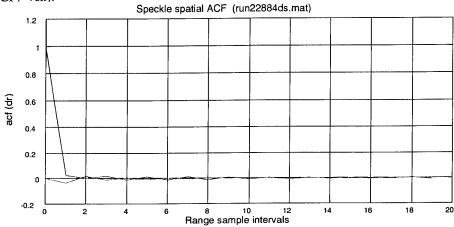


Figure 59: Speckle spatial correlation function for run22884 data set [Im (SACF)- green, Re (SACF)- red].

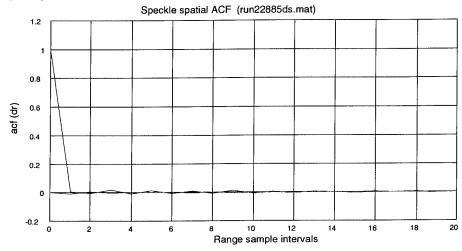


Figure 60: Speckle spatial correlation function for run22885 data set [Im (SACF)- green, Re (SACF)- red].

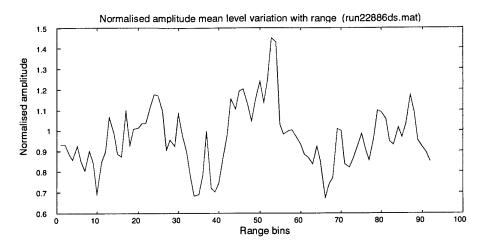


Figure 61: Typical range profile of clutter mean level for run22886 data set (upwind/upswell). Grazing angle 1.14°.

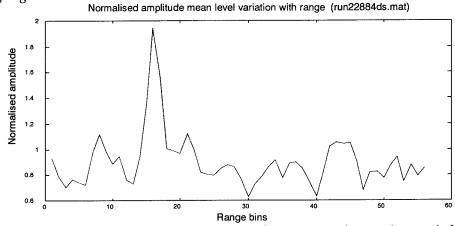


Figure 62: Typical range profile of clutter mean level for run22884 data set (cross-wind/cross-swell). Grazing angle 2.37°.

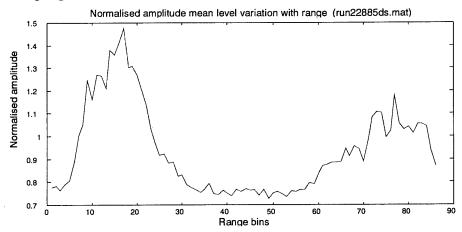


Figure 63: Typical range profile of clutter mean level for run22885 data set (intermediate look direction). Grazing angle  $0.59^{\circ}$ .

a much smaller variation about the mean, as expected with the larger grazing angle and cross-swell viewing direction.

The data in Figure 63 was obtained looking at the intermediate direction (135°) relative to the wind/swell direction with a grazing angle of 0.59° and at a range of 17.5 km. The range profile shows a very strong periodicity due to a heavy swell that was observed during the data collection period.

The texture value at each range was estimated by squaring the data from (3.40). Then the texture spatial ACF was obtained by averaging the spatial ACFs of a number (*J*) of successive profiles:

$$\hat{S}_{y}[l] = \frac{1}{JK} \sum_{j=1}^{J} \hat{S}_{y_{j}}[l] = \frac{1}{JK} \sum_{j=1}^{J} \sum_{k=1}^{K-l} \hat{y}_{j}[k] \hat{y}_{j}[k+l]$$
(3.41)

The first 40 terms of the normalised spatial ACFs of the analysed data sets, estimated according to (3.41), are shown in Figures 64-66. It can be seen that data sets which were collected in the upswell/upwind (Figure 64) and intermediate relative to the swell/wind (Figure (66) look directions are characterized by much longer range correlation length compared to that for the data set that was collected in the cross-swell/cross-wind look direction (Figure 65). As the spatial correlation properties of the texture reflect the dynamics of the sea surface, it is reasonable to assume that they are independent of grazing angle.

Figures 67-69 present the texture normalised spatial covariance functions of the analysed data sets to better illustrate periodic variations of the mean clutter level with the look direction angle relative to the wind/swell direction change that were observed during the data collection. The autocovariance function is determined as

$$\hat{Q}_{y}[l] = \frac{1}{JK} \sum_{j=1}^{J} \sum_{k=1}^{K-l} (\hat{y}_{j}[k] - \overline{y}_{j}) (\hat{y}_{j}[k+l] - \overline{y}_{j}) = \frac{1}{J} \sum_{j=1}^{J} (\hat{S}_{y_{j}}[l] - \overline{y}_{j}^{2})$$
(3.42)

where  $\overline{y}_{j}$  is the texture mean value in j -th range profile given by

$$\overline{y}_j = \frac{1}{K} \sum_{k=1}^K \hat{y}_j[k] \tag{3.43}$$

The first 40 terms of the averaged normalised range covariance function for the three analysed data files are shown in Figures 67-69. It can be seen that the form of this function is different in each case. Data files run22886 and run22885 (Figures 67 and 69) contain clutter with a long periodic fluctuation due to a heavy swell, while at the other extreme, file run22884 (Figure 68) represents clutter with little spatial correlation.

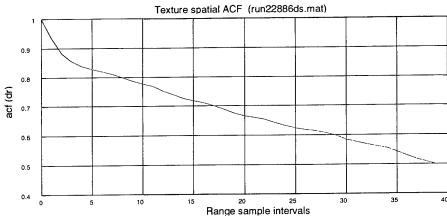


Figure 64: Texture spatial correlation function for run22886 data set (upwind/upswell).

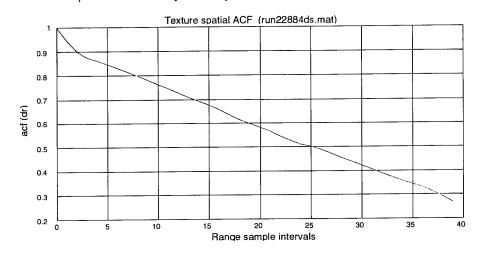


Figure 65: Texture spatial correlation function for run22884 data set (cross-wind/cross-swell).

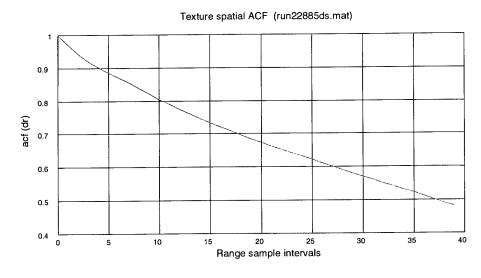


Figure 66: Texture spatial correlation function for run22885 data set (intermediate look)

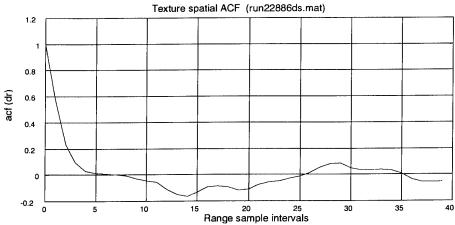


Figure 67: Texture spatial covariance function for run22886 data set (upwind/upswell).

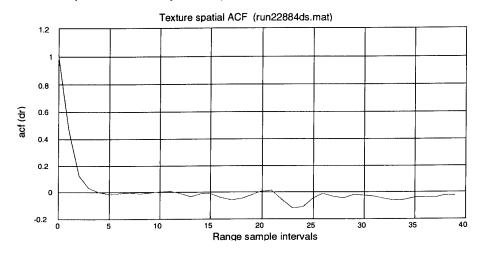


Figure 68: Texture spatial covariance function for run22884 data set (cross-wind/cross-swell).

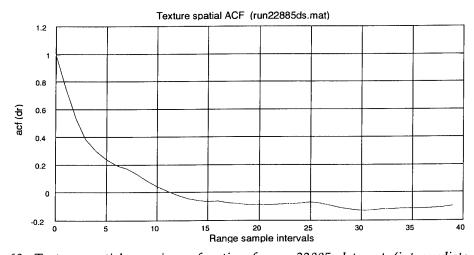


Figure 69: Texture spatial covariance function for run22885 data set (intermediate look direction).

Looking into the swell (Figure 67), the radar resolves structure larger than the 1.5 m that corresponds to the radar range resolution. Therefore, in this case range correlation uncovers the structure of the sea surface (the spatial ACF clearly shows the presence of wave structure). Across the swell (Figure 68), the wide cross-range footprint of the radar is aligned perpendicular to the incoming swell and there is a suppression of wavelike patterns travelling parallel to the radar line of sight. In the case of the transmit geometry with intermediate look direction (Figure 69), the relatively wide cross-range footprint of the radar is no longer perfectly aligned perpendicular to the incoming swell, and thus, with wavelengths on the order of tens of meters, includes a mixture of crests and troughs.

It was shown [41] that for a fully developed sea the correlation length  $\rho$  of the sea surface in the range direction is taken to be a length characteristic of wind waves, given in terms of wind velocity  $W_V$  and g, the acceleration due to gravity and it can be determined as:

$$\rho = \frac{\pi}{2} \frac{W_v^2}{g} (3\cos^2\theta + 1)^{1/2}$$
 (3.44)

where  $\theta$  is the angle between the line of sight and the wind direction.

If the radar range resolution is  $\Delta R$ , the correlation length, expressed in radar range samples (the number of samples after which the clutter may be said to be significantly decorrelated) is

$$R_{cor} = \rho / \Lambda R \tag{3.45}$$

Table 17 presents the measured values of correlation length of the sea surface in the range direction, expressed in radar range samples, and the corresponding values calculated using (3.44) – (3.45) for a fully developed sea and the given radar range resolution (1.5 m).

Table 17: Spatial correlation of sea clutter.

Run ID	Look direction angle relative to the wind direction	Correlation length predicted, ho (m)	Predicted $R = \frac{\rho}{\Delta R},$ $\Delta R = 1.5 m$	Correlation length measured, $\rho_m$ (m)	Measured $R_m = \frac{\rho_m}{\Delta R},$ $\Delta R = 1.5 m$
22886	0	9.69	6	11.25	7
22884	270	4.85	3	5.25	3
22885	135	7.67	5	15.75	10

The comparison of measured and predicted spatial correlation lengths for a fully developed sea indicates that the analysed data were collected under conditions of changing wind speed before the wind-generated waves were fully developed. This

observation is in agreement with the data presented in Section 2.4. The difference between measured and predicted sea spatial correlation lengths is largest for run22885 data set. It can be explained by a particular heavy swell that was observed during this data collection period.

3.4.2.2.3 Comparison of Model - Based and Nonparametrically Estimated Intensity Spatial Autocorrelation Functions

Figures 70-72 present the results of comparison of the clutter intensity normalised spatial ACF obtained by using the compound K-distribution model that is described by equations (3.35) – (3.39) with the overall normalised spatial ACF nonparametrically estimated from a single range profile data z[n] for each analysed data set.

It can be seen that the model-based and nonparametrically estimated normalised spatial ACFs of the sea clutter intensity are very similar for each analysed data set. The peak due to speckle correlation is evident.

### 3.5 Spectral Analysis

The high-resolution radar interrogates only a limited portion of the long-wave surface, but the signal is still the sum of a large number of returns due to the capillary waves. Ocean radar scattering at small grazing angle generally yields Doppler spectra with a peak in the VV returns near the Bragg resonant frequency but skewed toward higher frequencies. On the other hand, the HH Doppler spectra generally show a peak at a much higher frequency than the VV peak frequency, but skewed toward lower frequency. At small grazing angles, in addition to Bragg scattering, the returns are also strongly influenced by scattering from fast events (probably from wave crests of longer waves), which occur sporadically in time. The scattering can thus be "lifetime dominated" as well.

These results provide compelling evidence that several entirely different physical mechanisms, corresponding to different features of the dynamic sea surface, actively contribute to microwave backscatter returns. According to the latest research [27, 28 – 31, 49], the mechanisms are:

- Scattering from free Bragg waves, characterized by a Gaussian distribution in scatterer speeds and a Gaussian component in the power spectral density (PSD),
- Scattering from sporadically-appearing, fast moving, short lifetime, facet-like scatterers, characterized by an exponential distribution in scatterer lifetime and a Lorentzian component in the PSD,
- Scattering from fast scatterers, which have a spread in speeds, characterized by a convolution of the Gaussian and Lorentzian processes, resulting in a Voigtian component in the PSD.

Therefore, it can be accepted that the return from the moving sea surface is a result of the interaction of different types of returns from a large number of individual scatterers

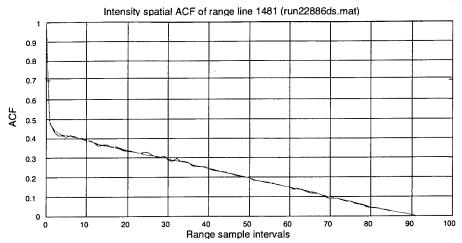


Figure 70: Intensity spatial correlation function for run22886 data set [model-based - green, nonparametrically estimated - red].

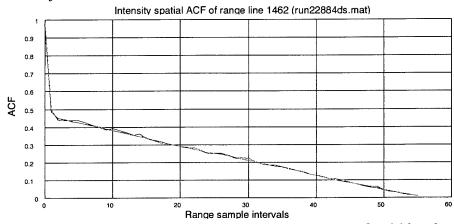


Figure 71: Intensity spatial correlation function for run22884 data set [model-based - green, nonparametrically estimated - red].

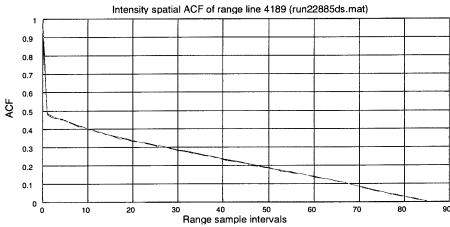


Figure 72: Intensity spatial correlation function for run22885 data set [model-based - green, nonparametrically estimated - red].

distributed over the area of the sea surface within the range cell being considered. As a consequence, the number of scatterers, or equivalently, the received power, is not constant, but depends upon both the electromagnetic and the geometric (the orientation of the scatterers with respect to the radar antenna) characteristics of the illuminated patch.

### 3.5.1 Frequency-Time Analysis

The geometry of the surface is space and time varying and a fixed orientation of the scatterers from observation to observation is not reasonable in general [46]. Thus, although the total number of scatterers can be fixed once and for all, only a random fraction K(t) of these are effective, in the sense that they produce a nonzero return. The number of scatterers  $K(t_1)$  and  $K(t_2)$ , measured at two time instants  $t_1$  and  $t_2$  are correlated; in other words, K(t) does not simplify either to a sequence of independent random variables or a constant function. It can be shown [46] that the discrete random variate K(t) can be presented as having the compound-Poisson distribution that arises from a random Poisson sum of independent variates.

Transmitting a sinusoid signal, the echo from K(t) scatterers located at positions  $r_k(t)$  at the sea surface within a range cell can be presented as

$$s_{c}(t) = \sum_{k=1}^{K(t)} A_{k}(t) s \left( t - \frac{2 r_{k}(t)}{c} \right) = \exp \left\{ j 2 \pi f_{0} t \right\} \sum_{k=1}^{K(t)} A_{k}(t) \exp \left\{ - j \frac{4 \pi r_{k}(t)}{\lambda} \right\}$$
(3.46)

where  $A_k(t) < 1$  is the amplitude reduction factor due to scattering and propagation losses, c is the speed of light and  $\lambda$  is the radar wavelength.

When transmitting a chirp signal, a similar expression can be written for each frequency component in the transmitted chirp.

The time-varying distance between the radar and the k-th scatterer on the sea surface  $r_k(t)$  (k = 1, ..., K(t)) can be approximated as

$$r_k(t) = r_{0c}(t) + v_{yk}t + \frac{1}{2}\left(a_{yk} + \frac{v_{xk}^2}{r_{0c}}\right)t^2 + \frac{1}{2r_{0c}}a_{xk}v_{xk}t^3 + \frac{1}{8}a_{xk}^2t^4 + \dots$$
(3.47)

where  $r_{0c}(t)$  is the distance between a radar and a range cell,  $v_{yk}$  is the radial velocity of the k-th scatterer,  $a_{yk}$  is the k-th scatterer radial acceleration,  $v_{xk}$  is the k-th scatterer cross-range velocity,  $a_{xk}$  is the k-th scatterer cross-range acceleration.

The phase of the overall clutter response (3.46) is determined by the vector sum of returns from a large numbers of ever-changing reflectors with different motion parameters on a patch of the sea surface.

Using (3.46) the received signal from each range cell on the sea surface after demodulation is given by

$$w(t) = \sum_{k=1}^{K(t)} A_k(t) \exp\left\{-j \frac{4\pi r_k(t)}{\lambda}\right\} + n(t)$$
 (3.48)

An essential point to note is that the spectrum of sea clutter is likely to vary quite significantly with range, associated with the spatial variation of the underlying mean level [50]. Analysis of experimentally collected sea clutter data [29, 31, 36, 48, 49] has shown that the form of sea clutter spectrum is predominantly determined by the swell structure in the sea surface and additionally affected by the presence of local discrete events of various forms on the sea surface that change velocity with time. There are several explanations for this velocity change:

- A physical velocity change could arise from a wave changing through acceleration by a wind gust;
- An event could be compound. For example, a ripple travelling upon a large wave;
- The event could expose a different velocity component of itself by breaking;
- The radar could show some transition between imaging two different events of differing velocity.

It is reasonable to assume that several events are occurring simultaneously at different velocities due to extent of the range cell. Therefore, the normalised form of the sea clutter spectrum is not constant, but has a range and time variable shape and Doppler shift.

The instantaneous Doppler frequency (IDF) of the clutter reflected signal (3.48), assuming that the derivatives of the amplitude terms are negligible, is determined as [47]

$$f_{I}(t) = \frac{\sum_{k=1}^{K(t)} A_{k}(t)^{2} f_{I_{k}}(t) + \sum_{k,j=1[k \neq j]}^{K(t)} q_{k,j}(t) \left( f_{I_{k}}(t) + f_{I_{j}}(t) \right)}{\sum_{k=1}^{K(t)} A_{k}(t)^{2} + \sum_{k,j=1[k \neq j]}^{K(t)} q_{k,j}(t)}$$
(3.49)

where

$$f_{I_k}(t) = \frac{2}{\lambda} \frac{dr_k(t)}{dt} \text{ is the } k \text{-th scatterer IDF}; \quad q_{k,j}(t) = A_j(t) A_k(t) \cos \left( \frac{4\pi r_k(t)}{\lambda} - \frac{4\pi r_j(t)}{\lambda} \right).$$

Hence, it is necessary to estimate the sequence of sea clutter Doppler spectra as it changes with range and time.

The consecutive "instantaneous" Doppler spectrum estimates can be calculated from sequential and possibly overlapping segments of the sampled backscattered signal, which correspond to the returns from a single range cell over many consecutive pulses [37, 47].

Thus, the short-time Fourier transform (STFT) algorithm estimates the sea clutter Doppler spectrum as it varies with the sliding window sample number in the signal sequence ( $k_W$ ):

$$F_{m_R}(k_W, l_F) = \sum_{n=1}^{N} w_{m_R}(n, k_W) u(n) \exp\left\{-j \frac{2\pi (n-1)(l_F - 1)}{N}\right\}, \quad (3.50)$$

$$l_F = 1, ..., N; k_W = 1, ..., K_W; m_R = 1, ..., M_R$$

where  $K_W$  is the number of N point sliding windows along the signal time sequence in a range bin;  $M_R$  is the number of range bins; u(n) is the N point symmetric Hanning window and  $w_{m_R}(n,k_W)$  is the n-th pulse complex signal in a  $k_W$ -th sliding window.

The discrete variable,  $l_F$ , is related to frequency (in Hz) by the following expression:

$$f = \frac{l_F - 1}{N\tau_s} \tag{3.51}$$

where  $\tau_s$  is the PRI.

For *N* clutter returns in each sliding window the energy of the 'instantaneous' spectrum is distributed over several contributing components and, hence, the STFT provides a relatively wide spectrum with a peak value at the dominant component IDF, the value of which changes with time (i.e. with the sliding window sample number).

To confirm this statement for the experimental sea clutter data collected during the ESRL 38/97 trial, the STFT analysis was applied to the sea clutter signals reflected from a single azimuth line (range cell) of the following data sets:

- run22886 that corresponds to the upswell/upwind look direction,
- run22884 that corresponds to the cross-swell/cross-wind look direction, and
- run22885 that corresponds to the intermediate look direction, respectively.

The short-time Fourier transforms (STFTs) in each range cell were observed over short time periods (N =128 pulses sliding window with 75% overlap).

Figures 73 - 75 present the results of the STFT analysis for a single range cell from each considered data set. It can be seen that the energy within the return is spread out over a large portion of the spectrum and the position of the maximum peak value changes with time.

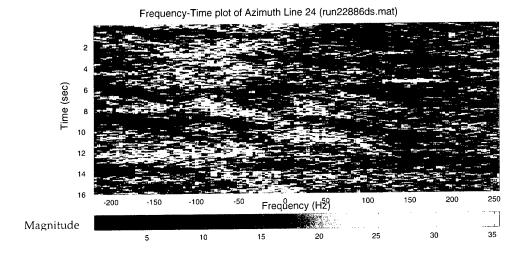


Figure 73: Frequency-time analysis for a single range cell from run22886 data set.

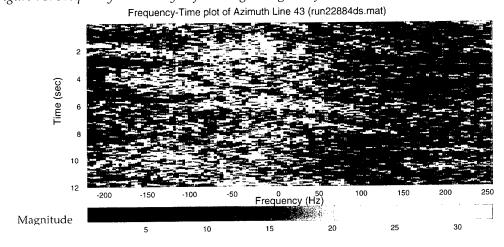


Figure 74: Frequency-time analysis for a single range cell from run22884 data set.

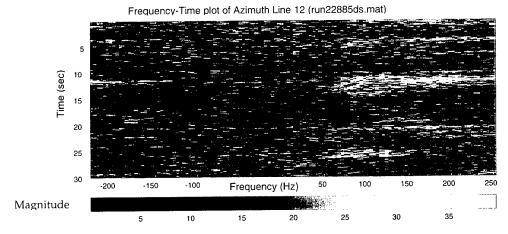


Figure 75: Frequency-time analysis for a single range cell from run22885 data set.

Figures 76 - 78 present the results of the STFT frequency-time analysis for the data sets run2286, run2284 and run2285, respectively:

$$f_{l}(k_{W}, m_{R}) = \log_{10} \left[ \max_{l_{F}} \left\{ F_{m_{R}}(k_{W}, l_{F}), l_{F} = 1, ..., N \right\} \right]$$
 (3.52)

It can be seen that the peak values of 'instantaneous' transforms performed by using returns from range cells containing sea clutter over many consecutive pulses change considerably, and this change corresponds to the large scale structures of the sea surface.

Two additional conclusions that can be drawn from the frequency-time analysis of the collected spiky VV-polarised sea clutter data are similar to those presented in the literature for sea clutter at low grazing angles and high range resolution [5, 6, 10, 15, 29, 38]:

- During the periods of strong radar returns associated with spiky sea clutter at low grazing angles and high range resolution, the power spectrum exhibits a characteristic significant high frequency component.
- It appears to be a correlation between the overall magnitude of a spatially and temporally extended spiking event, and how high in frequency the significant high frequency spectral components are found.

## 3.5.2 Averaged Doppler Spectrum Analysis

It was shown [27 – 31, 49] that the averaged Doppler power spectrum  $\Phi_{VV}(f)$  for sea clutter signals having VV polarization, (and verified in our collected data), at small grazing angles is often asymmetric and can be well fitted by a dominant Gaussian component, representative of Bragg scattering, peaked at a low frequency and an unresolved Voigtian component at a somewhat higher frequency:

$$\Phi_{VV}(f) = B_f \Phi_B(f) + F\Phi_F(f), \tag{3.53}$$

where  $B_f$  and F indicate Bragg and faster-than-Bragg components, respectively. The coefficient  $B_f$  is set using the composite surface Bragg scattering model [27, 29], and the coefficient F describes the relative strength of the non-Bragg contribution that moves at the phase speed of the "most-likely to break" waves. (Note that the "most-likely to break" waves are not the dominant waves of the ocean wind-wave spectrum as it is for the wavetank experiments [29, 31, 49]).

An important consideration in the X-band range of frequencies is that sea spike coverage at low grazing angles and high range resolution depends to a large extent upon surface features not yielding whitecap signatures. The majority of radar sea spikes do not correspond to whitecaps, but to small, "steep" features.

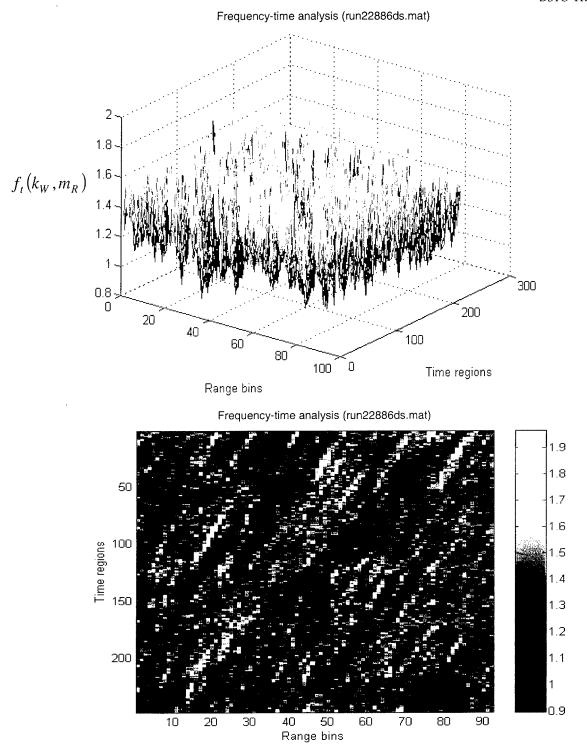
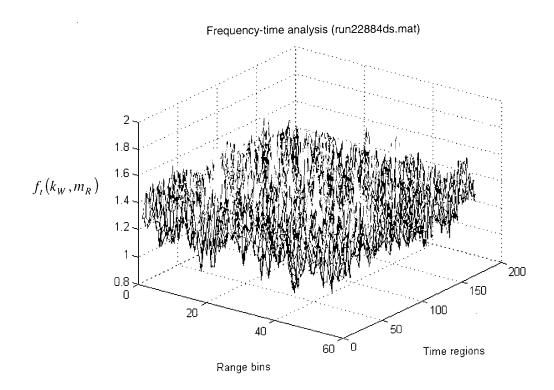


Figure 76: Frequency-time analysis for run22886 data set ( $log_{10}$  intensity scale).



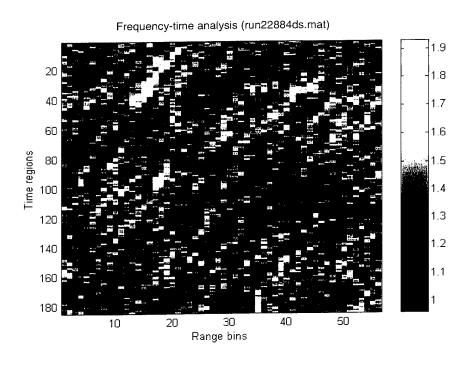


Figure 77: Frequency-time analysis for run22884 data set ( $log_{10}$  intensity scale).

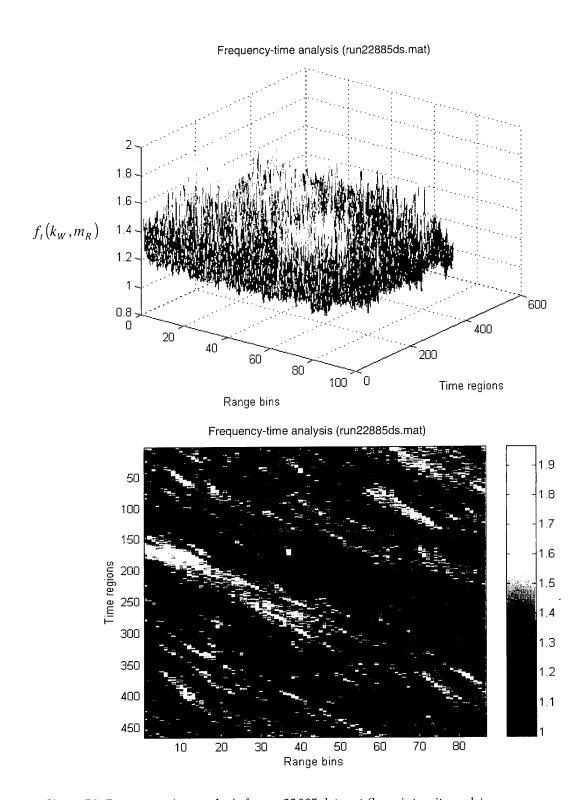


Figure 78: Frequency-time analysis for run22885 data set ( $log_{10}$  intensity scale).

Thus, for the upwind look direction in conditions of a fully developed sea the sea spike fractional coverage (i.e. the average fraction of radar image pixels occupied by sea spike events) varies approximately quadratically with the friction velocity  $u_*$  [32].

The value of coefficient *F* depends on the angle of the look direction relative to the wind direction: it is highest for the upwind look direction and equal to zero for the cross-wind look direction [29].

The Doppler power spectra of the Bragg component having a Gaussian lineshape, and the faster-than-Bragg component having a Voigtian lineshape that is characterized by a convolution of the Gaussian and Lorentzian profiles [28-30], are described as:

$$\Phi_B(f) = \frac{1}{f_{BW}\sqrt{\pi}} \exp\left[-\frac{(f - f_B)^2}{f_{BW}^2}\right],\tag{3.54}$$

$$\Phi_{F}(f) = \frac{\Gamma}{2\pi^{2} f_{PW}} \int_{-\infty}^{\infty} \frac{\exp(-y^{2})}{\left[\frac{(f - f_{P})}{f_{PW}} - y\right]^{2} + \left(\frac{\Gamma}{2\pi f_{PW}}\right)^{2}} dy, \qquad (3.55)$$

where  $f_B$  and  $f_P$  are the frequencies corresponding to the Bragg resonant wave speed and the "most-likely to break" wave phase speed, respectively;  $f_{BW}$  and  $f_{PW}$  are the Doppler spectrum widths of each of the spectral components;  $\Gamma^{-1}$  is the characteristic scatterer lifetime. The widths of each of the spectral components  $f_{BW}$  and  $f_{PW}$  in equations (3.54) and (3.55) are left as free parameters to be varied to get the best fit to the data.

The composite surface theory can describe the scattering processes of the slow (Bragg) portion of the Doppler spectrum. This theory decomposes a rough air-water interface into small-scale and large-scale features. Small-scale features may be highly irregular but are assumed to have small slopes and displacements. The irregular nature of this small-scale structure causes it to decorrelate very rapidly in time and space so that small segments, or facets, of this surface may be considered individually. Large-scale features are assumed to have curvatures small compared to the inverse of the small-scale decorrelation length so that they may be considered planar over these scales. Small-scale slopes and displacements are all measured relative to this large-scale surface. Thus the large-scale surface displaces correlated segments of the small-scale features, tilts them, and possibly changes their amplitude. Furthermore, any currents associated with the large-scale surface affect the segments of small-scale surface like corks floating on the large-scale surface [35].

Under these hypotheses, microwave scattering occurs because of resonant Bragg scattering from capillary (small-scale) waves on the water surface. For backscatter, the resonant condition is:

$$\lambda_B = \frac{\lambda}{2\cos\theta_g} \,\,\,\,(3.56)$$

where  $\lambda_B$  is the short, Bragg-resonant wave responsible for the scatter, and  $\theta_g$  is the radar local grazing angle. Typical patterns from microwave antennas illuminate areas of ocean surface, which are large compared with  $\lambda_B$  in both dimensions. In these conditions, only short waves propagating rapidly toward or away from the antenna backscatter to the antenna [35].

Then the phase speed of the water wave associated with the underlying water level is determined via the gravity-capillary dispersion relation as

$$c_{Bp} = \sqrt{\frac{g}{k_B} + \frac{\gamma}{p} k_B} , \qquad (3.57)$$

where  $k_B = \frac{4\pi \cos\theta_g}{\lambda}$  is the Bragg-resonant wavenumber in water, g is the gravitational acceleration,  $\gamma$  and p are the water surface tension and density, respectively.

The standard equation for the Doppler shift,  $f_D$ , induced in backscattered microwaves due to surface moving with a line-of-sight velocity  $v_R$  toward or away from the antenna is:

$$f_D = \frac{2v_R}{\lambda},\tag{3.58}$$

where  $\lambda$  is the microwave free space wavelength.

If the scattering is a Bragg-resonant phenomenon, then the line-of-sight velocity  $v_R$  is composed of the sum of the line-of-sight velocity of the aircraft antenna  $v_a$ , any large-scale, line-of-sight velocities of the sea surface movement V and the component of the intrinsic phase speed,  $c_{Bp}$ , of the Bragg wave along the line of sight.

Note that if during the data collection process the distance from the aircraft to the swath was kept constant for each run, the line-of-sight velocity of the aircraft antenna  $v_a$  would be equal to zero for all runs as the antenna was pointed at -90° relative to the direction of aircraft movement (see Section 2.5). But the surface range to the swath and the aircraft altitude above the earth surface varied pulse-to-pulse due to deviation of the aircraft from the ideal track. Therefore the line-of-sight velocity of the aircraft

antenna  $v_a$  has to be calculated using the values of these parameters that can be read from the auxiliary data exactly for each pulse.

It was shown [29, 31, 49] that the free Bragg waves are generated after the wave has broken. They are located near the crest of the broken gravity wave and are strongly affected by the orbital motion of the underlying gravity waves, i.e. small Bragg resonant ripples are modulated by the drift velocity of the dominant gravity waves  $c_d$ . For open waters, a form for this component, which has been found to successfully describe the experimental data for upwind look direction, is the solution to the Stokes equation [27]:

$$c_d = \Omega K \left(\frac{H}{2}\right)^2 \frac{\cosh 2Kd}{2\sinh^2 Kd},\tag{3.59}$$

where  $K = \frac{2\pi}{\lambda_d}$  is the wavenumber of the dominant gravity waves in the wind-wave

field,  $\lambda_d$  is the wavelength of the dominant gravity waves,  $\Omega$  is the angular frequency of the dominant gravity waves, H is their trough to crest height and d is the water depth. Research has shown that a good approximation to this drift is 2.6-5.5% of the wind speed [29].

Thus, for constant large-scale currents, or none at all, the overall speed of the Bragg scatterers is given by

$$c_B = V \pm c_{Bp} = c_d \pm c_{\epsilon} \pm c_{Bp} , \qquad (3.60)$$

where and  $c_{c}$  is the current velocity (that is assumed to be zero).

Therefore, the measured Doppler frequency of the low-frequency peak of the VV polarization Doppler spectrum corresponding to the Bragg resonant wave speed can be presented for the upwind look direction as [29]

$$(f_{Dslow})_{upwind} = f_B = \frac{2\cos\theta_g}{\lambda} (v_a \pm c_B) = \frac{2\cos\theta_g}{\lambda} [v_a \pm (c_d \pm c_c \pm c_{Bp})], \quad (3.61)$$

We can obtain an approximation to the corresponding "slow"peak Doppler frequency dependence on the look direction relative to the wind direction using the results of research presented in [36, 43], which show that sea clutter data for both polarizations has a cosinusoidal dependence on the direction of the wind, with the smallest Doppler offset when looking across-wind.

Then the "slow" peak Doppler frequency is determined as:

$$f_{D_{slow}}(\theta) = f_B(\theta) = \frac{2\cos\theta_g}{\lambda} \left[ v_a \pm c_B(\theta) \right] = \frac{2\cos\theta_g}{\lambda} \left[ v_a \pm c_{Bp} \pm (c_d \pm c_c) \cos\theta \right], (3.62)$$

where  $\theta$  is the angle between the line of sight and the wind direction.

Thus a microwave Doppler spectrum due to Bragg backscattering is expected to exhibit two peaks located at  $f_B(\theta) = \frac{2\cos\theta_g}{\lambda}(v_a \pm c_B(\theta))$  corresponding to Bragg waves travelling toward or away from the antenna.

It is essential to note that at small grazing angles the rough sea state renders these peaks unresolvable in the X-band sea clutter spectrum:

- For the upwind look direction and wind speeds above ~ 6 m/s, the contribution
  due to receding Bragg waves is not usually observed, and only the "slow" peak
  corresponding to approaching Bragg waves is prominent [31];
- For the cross-wind viewing direction, the peak maybe slightly upshifted or downshifted from the "reference frequency"  $v_a$  depending on whether approaching or receding Bragg waves, respectively, are dominant in contributing to the backscatter return [29]. If both approaching and receding Bragg waves are equal, then the appropriate broadening of the Doppler spectrum about the "reference frequency"  $v_a$  is observed.

Analysis of the ocean scattering data at microwave frequencies has indicated that the faster-than-Bragg portion of the Doppler spectrum at small grazing angles is due to the breaking water waves that are the source of non-Bragg nature fast scatterers. It was shown [29, 31, 32, 49] that:

- For cross-wind viewing directions, the "slow" and "fast" peak separation does
  not occur for low grazing angles; i.e., both the VV and HH spectra peak at more
  or less the same low frequency corresponding to the Bragg resonant wave
  speed and the high-frequency peak of the Doppler spectrum is not observed;
- The surface geometry of a breaking wave contains scattering elements that can
  provide not only specular-like reflection from curved water facets, but also
  multiple scattering, which may or may not include a reflection at the Brewster
  angle;
- The crest region of the breaking waves is the principal source of the non-Bragg scattering phenomena. The high-frequency peak of the Doppler spectrum corresponds to the scattering from bound-Bragg waves and/or from facets (or wedges) and from sporadically appearing, short-duration (life-time dominated) "single-speed" objects near the crest region of a breaking wave such as nondegenerate facets;
- The speed of fast scatterers corresponds to the phase speed of a breaking wave since fast scatterers are located at the crest portion of a breaking wave;
- The phase speed of the "most-likely to break" wave associated with the fast scatterers grows approximately exponentially with increasing friction velocity; and
- The wavelength of the "most-likely to break" ocean wave is always much shorter than the dominant gravity wavelength of the ocean wind-wave

spectrum. These shorter gravity waves are "riding" on longer dominant waves, and they are modulated by the dominant waves to break.

Thus, the phase speed of the "most-likely to break" wave for a given wind speed can be determined using the approximation proposed in [31]:

$$c_p = c_0 \exp\left(\frac{u_*}{u_0}\right) \tag{3.63}$$

where:

 $u_*$  is the friction velocity that has to be determined from the following equations:

$$W_V = \frac{u_*}{k} \ln \left( \frac{z}{z_0} \right), \tag{3.64}$$

$$z_0 = \frac{0.684}{u_*} + 4.28 * 10^{-5} u_*^2 - 0.0443, \tag{3.65}$$

 $W_{v}$  is the wind speed at a height of 10 m,

 $W_V$  and  $u_*$  both have units of cm/s,

z is the height above the mean water level in cm,

k is von Karman's constant ( $k \approx 0.4$ ), and

 $c_0$  and  $u_0$  are coefficients, the values of which depend on the friction velocity:

$$c_0 = \begin{cases} 9.1 \ cm/s, \ if \quad u_* < 21 \ cm/s \\ 72 \ cm/s, \ if \quad u_* > 21 \ cm/s \end{cases}, \quad u_0 = \begin{cases} 8.5 \ cm/s, \ if \quad u_* < 21 \ cm/s \\ 53 \ cm/s, \ if \quad u_* > 21 \ cm/s \end{cases}$$
(3.66)

The "most-likely to break" wavelength can be calculated using the dispersion relation [31]:

$$\lambda_p = \frac{2\pi c_p^2}{g} \,, \tag{3.67}$$

Comparing (3.57) and (3.66) it can be seen that the Bragg-resonant wavelength is much shorter than the wavelength of the waves in the upwind look direction associated with the fast scatterers.

The high-frequency peak  $f_P$  in the X-band sea clutter Doppler spectrum at small grazing angles for the upwind look direction is determined by [29, 31]

$$(f_{D fast})_{upwind} = f_P = \frac{2 \cos \theta_g}{\lambda} [v_a \pm (c_d + c_p)],$$
 (3.68)

Note that this peak shifts to higher frequencies with increasing wind speed.

The approximation to the corresponding "fast" peak Doppler frequency dependence on the look direction relative to the wind direction is given by:

$$f_{D fast}(\theta) = f_P(\theta) = \frac{2 \cos \theta_g}{\lambda} \left[ v_a \pm \left( c_d + c_p \right) \cos \theta \right] . \tag{3.69}$$

Figures 79 - 81 present the Doppler spectra that are averaged over a sliding window with N = 128 pulses for a single range cell from each analysed data set.

Figures 82 – 84 show the Doppler spectra that are averaged over a sliding window with N = 128 pulses for all range cells of the considered data sets.

The upwind (Figures 79 and 82), intermediate (Figures 81 and 84) and cross-wind (Figures 80 and 83) spectral data confirm the fact that sea backscatter is not isotropic since waves propagate and also break predominantly in the wind direction.

For the upwind and intermediate look directions the Doppler spectra are asymmetric and cannot be well fitted by only a dominant component centred at the maximum of the spectra as they have a smaller unresolved component at a higher frequency. The Doppler frequency at the "slow peak" corresponds reasonably well to that given by (3.64), with the speed of the scattering object on the water surface matching the phase speed of the Bragg resonant water wave. The "fast peak" corresponds to scatterers, which move at speed much faster than the Bragg wave speed, and these faster scatterers are associated with the phase speed of a "most-likely to break" wave.

A cross-wind run means that the radar is looking perperdicular to the propagation direction of the dominant wave. For the cross-wind look direction, the radar does not collect (or very seldom collects) signals reflected by breaking waves and, therefore, a prominent fast component does not present in the Doppler spectra.

Table 18 summarises the results of Doppler spectra analysis for all the considered data sets together with environmental and computed data.

*Table 18: The results of Doppler spectra analysis for the considered data sets* 

	$\theta_g$	$v_a$	$W_{_{\scriptscriptstyle{\mathcal{V}}}}$	$c_p$	$c_{Bp}$	$c_d$	Calc.	Calc.	Calc.	Meas	Meas
Run ID	deg.	m/s	m/s	m/s	m/s	m/s	$f_{Dslow-}$	$f_{Dslow+}$	$f_{Dfast}$	$f_{Dslow}$	f <sub>D fast</sub>
							Hz	Hz	Hz	Hz	Hz
run22886	1.14	-0.8	5.7	1.06	0.23	0.3	-24.80	-53.8	-93.93	-51	-98
run22884	2.38	-1.4	5.9	1.06	0.23	0.3	-72.96	-101.9	n/o	-102	n/o
run22885	0.60	1.2	6.1	1.06	0.23	0.3	71.19	100.12	132.57	100	135

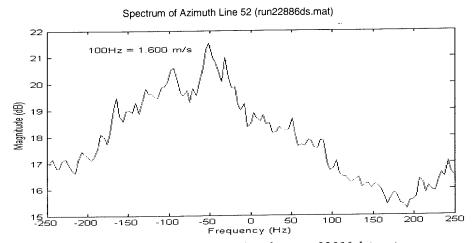


Figure 79: Sea clutter spectrum for an azimuth line from run22886 data set.

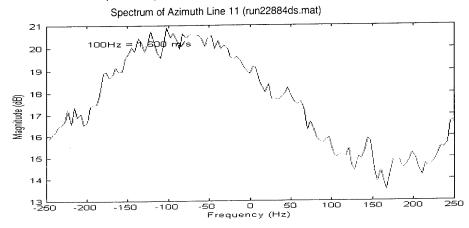


Figure 80: Sea clutter spectrum for an azimuth line from run22884 data set.

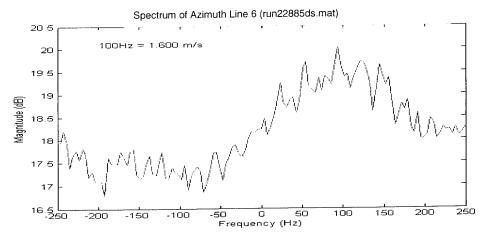
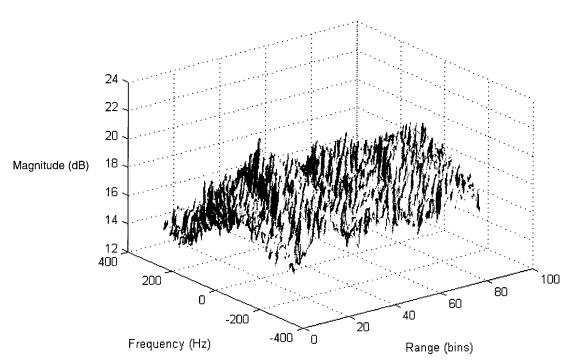


Figure 81: Sea clutter spectrum for an azimuth line from run22885 data set.





### Frequency analysis (run22886ds.mat)

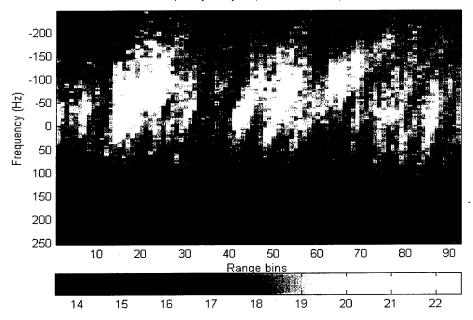
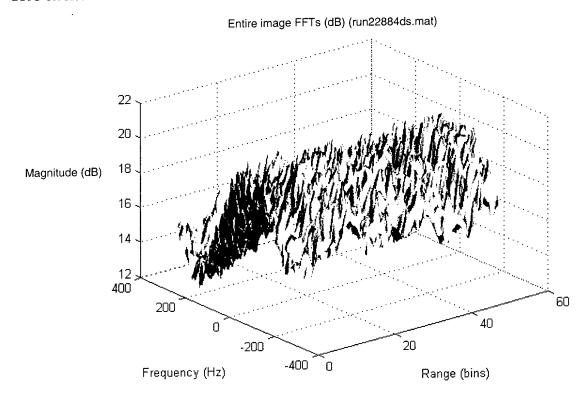


Figure 82: Averaged sea clutter spectra for run22886 data set.



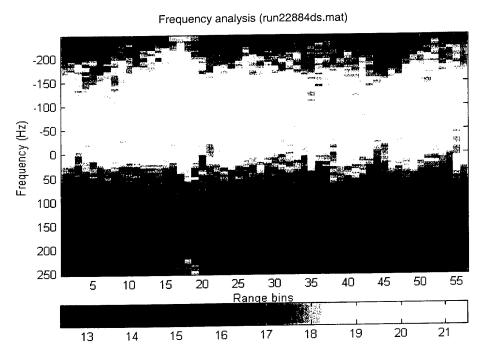


Figure 83: Averaged sea clutter spectra for run22884 data set.

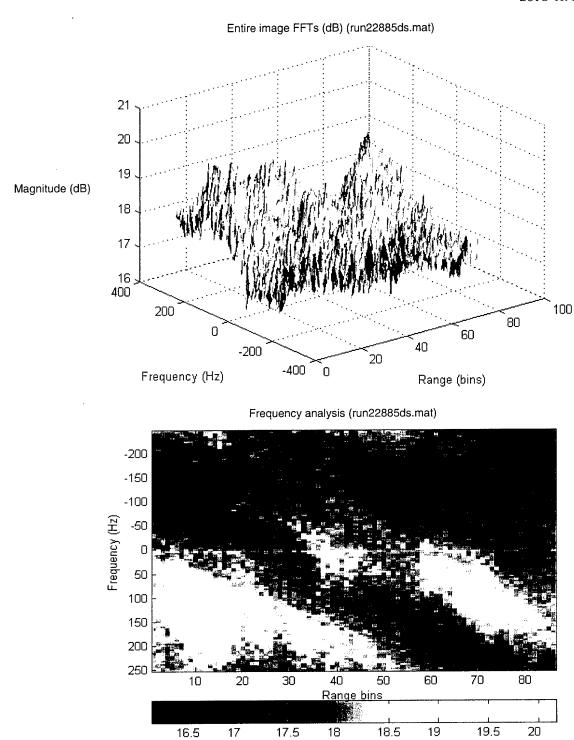


Figure 84: Averaged sea clutter spectra for run22885 data set.

Thus, the large-scale wave phenomena, travelling at speeds roughly of the order of the predicted "most-likely to break" wave phase speed, and smaller scale wave phenomena, travelling at speeds roughly on the order of the predicted Bragg resonant wave speed, were observed with an upwind and intermediate transmit geometries. The cross-wind viewing geometry provides results that can be effectively described by Bragg scattering.

## 3.6 Range-Time-Intensity Plot Analysis

A useful tool in analysing sea clutter both spatially and temporally (for a time scale measured in seconds) is the range-time-intensity (RTI) plot [6, 36, 38]. This section of the report presents RTI plots of the experimentally collected high-resolution (1.5 m) sea clutter data that were taken from a number of consecutive range resolution cells in a given direction for an extended period of time (12, 26 and 30 seconds for corresponding Figures 79 - 81). The squared magnitudes of the resulting time series were summed over contiguous blocks of 100 samples. The result is time series with each point representing the average clutter magnitude over a 200 msec time interval. The RTI plots in Figures 79 - 81 represent the data collected from 92, 56 and 86 contiguous range resolution cells, respectively. To illustrate the dependence of the RTI plot structure on viewing aspect, which can be explained in terms of the radar footprint, the RTI plots are presented for the upswell/upwind (Figure 82), cross-swell/cross-wind (Figure 83) and intermediate look (Figure 84) directions.

The analysed data were collected under conditions of changing wind speed before the wind-generated waves were fully developed. As described in Section 2.4, the presence of the smaller-scale cross-structure in the form of substreaks within the large-scale streaks was observed during the data collection process. These substreaks, which only run from side to side of the larger streaks, had steep slopes and hence, smaller speeds. Occasional breaking waves on top of swell and froth patches (2 x 3m) on the backs of waves contributed to the reflection process.

For the upwind/upwind transmit geometry (Figure 82) the relatively wide cross-range footprint of the radar was aligned with the incoming swell, so that it alternately caught the more reflective crests and then the less reflective troughs associated with individual waves. Thus, when looking into the swell, the radar resolved structure greater than the radar range resolution (1.5 m). On the other hand, the wide azimuthal beamwidth tended to filter out those waves travelling perpendicular to the radar line of sight, through the interference of the returns from multiple independent scattering centers associated with the train of waves falling within the radar footprint [36, 38].

For the cross-swell/cross-wind transmit geometry (Figure 83) the wide cross-range footprint of the radar was aligned perpendicular to the incoming swell, and a suppression of wavelike patterns travelling parallel to the radar line of sight is evident. Across the swell, only structure greater than the cross-range resolution is resolved, and then not in range but in time as the swell moves through the beam. The cross-swell RTI plot is therefore not expected to show the wavelike pattern of the upswell RTI plot.

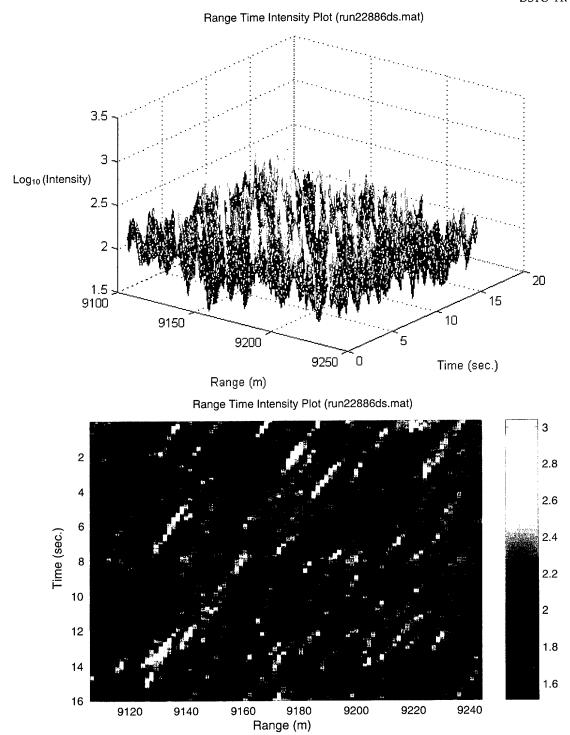


Figure 85: Range-time-intensity plot for run22886 data set ( $log_{10}$  intensity scale).

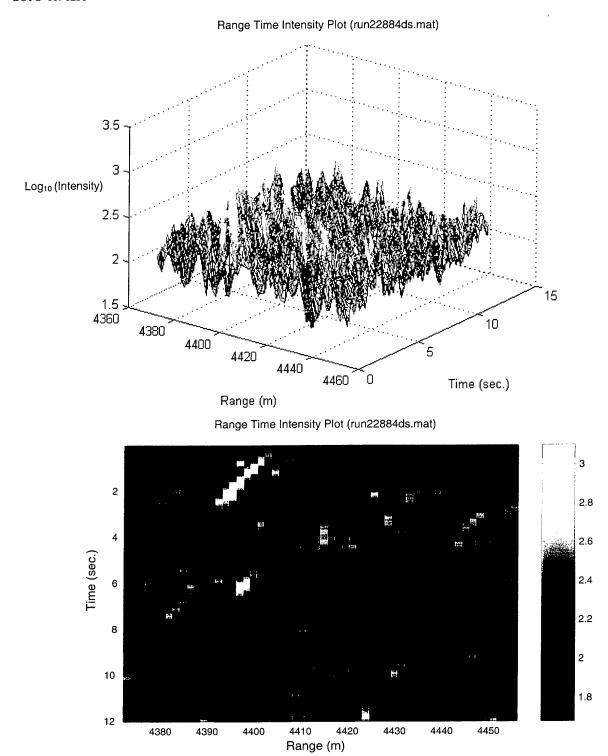
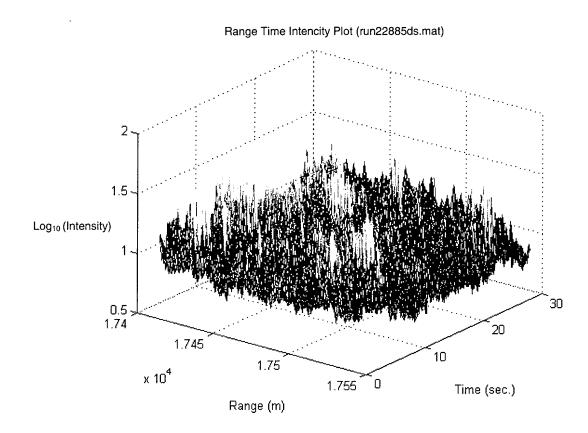


Figure 86: Range-time-intensity plot for run22884 data set ( $log_{10}$  intensity scale).



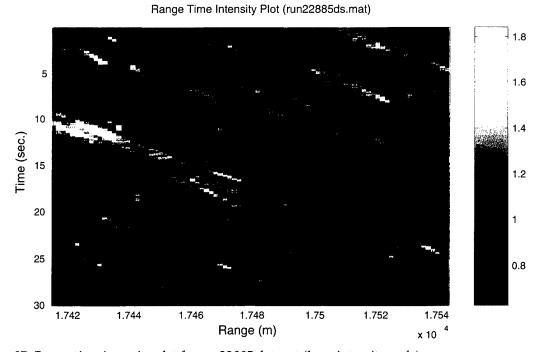


Figure 87: Range-time-intensity plot for run22885 data set (log<sub>10</sub> intensity scale).

The shorter correlation period but still fairly regular, wavelike pattern of the RTI plot is observed for the transmit geometry that was no longer aligned parallel with the wind and incoming swell, but which was also not completely perpendicular to them (Figure 84). The relatively wide cross-range footprint of the radar in this case included a mixture of crests and troughs.

# 4. Summary

This report describes the results of detailed statistical analysis of sea clutter data that were collected during the ESRL 38/97 trial, which was held off the Northern Australian coastline in February 1999. One of the trial's main objectives was to contribute to a database of experimentally collected clutter returns with radar system parameters that are comparable to those used in the Anti-Submarine Warfare mode of the Elta EL/M 2022A(V)3 maritime surveillance radar system.

The validity of the compound K-distribution model has been proven for the collected sea clutter data, both for amplitude and correlation properties.

It was shown that the K-distribution model provides the best fit to the experimentally collected data (of the most popular spiky sea clutter models (Log-Normal, Weibull and K-distribution) in the low probability of false alarm region). Among the K-distribution parameter estimation methods, the PDF with the parameters using Watts' method gives a better fit to the experimental amplitude histogram in the important low PFA region than the others.

As an accurate prediction of the radar detection performance is usually more dependent on the accurate modelling of temporal and spatial correlation features than on the choice of amplitude distribution [22, 23, 36], it is important that the K-distribution model provides proper handling of the temporal and spatial fluctuations of the collected sea clutter returns. It was shown that the K-distribution model-based and nonparametrically estimated normalised temporal and spatial ACFs of the sea clutter intensity are very similar to each other for each analysed data set.

The spectral analysis of the experimentally collected sea clutter data showed that several entirely different physical mechanisms, corresponding to different features of the dynamic sea surface, contribute to the spectral characteristics of sea clutter. For the upwind and intermediate look directions the Doppler spectra are asymmetric and cannot be well fitted by only a dominant component centred at the maximum of the spectra as they have a smaller unresolved component at higher frequency. The Doppler frequency at the "slow peak" corresponds reasonably well to the speed of the scattering object on the water surface matching the phase speed of the Bragg resonant water wave. The "fast peak" corresponds to scatterers that move at speeds much faster than the Bragg wave speed, and these faster scatterers are associated with the phase

speed of a "most-likely to break" wave. For the cross-wind look direction, the radar does not collect (or very seldom collect) signals reflected by breaking waves and, therefore, a prominent fast component does not present in the Doppler spectra.

For the successful estimation of the sea clutter characteristics in a process of prediction of the performance of the Anti-Submarine Warfare mode Elta EL/M 2022A(V)3 maritime surveillance radar system in Australian environmental conditions, further analysis of the experimentally collected sea clutter data needs to be done in order to:

- Clarify which mean sea clutter reflectivity model among the existing models [6, 8, 15, 18, 20, 45] provides the best results for Australian environmental conditions;
- Validate of the existing empirical models [7, 36, 45] for prediction of the K-distributed sea clutter shape parameter, which were proposed for a radar with the range resolution greater than 4 m and UK or Canadian environmental conditions, for the Anti-Submarine Warfare mode range resolution of the Elta EL/M 2022A(V)3 radar and Australian environmental conditions.

# 5. Acknowledgements

The author would like to thank James McCarthy and John Baldwinson, Surveillance Systems Division, DSTO, for the many helpful discussions, the ideas that have arisen from these discussions and for their help in preparation of Section 2 of this report.

## 6. References

- Haywood, B., McCarthy, J., Baldwinson, J., "ISAR Imaging and Sea Clutter Data Collection Trial ESRL 38/97", DSTO-DP-0428, 1999.
- 2. Antipov, I., McCarthy, J., Baldwinson, J., "Maritime Radar Data Collection Trial ESRL 38/97", DSTO-DP-0458, pp. 27, 1999.
- 3. Skolink, M., Radar Handbook, chap. 13.2 "Description of the Sea Surface", 2<sup>nd</sup> Ed., McGraw-Hill, 1990.
- 4. Nogara, T.J., Haykin, S., "Canadian East Coast Radar Trials and the K-distribution", IEE Proceedings-F, Vol. 138, No 2, pp. 80-88, 1991.
- 5. Chan, H.C., "Radar Sea-clutter at Low Grazing Angles", IEE Proceedings, Vol. 137, Pt. F, No 2, pp. 102-112, 1990.
- 6. Chan, H.C., "Analysis of the North Truro Sea Clutter Data", DREO, Report No.1051, pp.50, 1990.
- 7. Ryan, J., Johnson, M., "Radar Performance Prediction for Target Detection at Sea", Radar-92, IEE Conf. Proc. No 365, pp. 13-17, 1992.
- 8. Ryan, J., Johnson, M., "Modelling Radar Sea Clutter", Contract Report for DREO, W7714-9-9257/01-ST, pp. 62, 1990.
- 9. Nathanson, F., Cassaday, W., Barnes, C., Tuley, M., Williamson, F., Moore, L., "Airborne Clutter Measurements", IEEE International Radar Conference, pp. 60-65, 1993.
- 10. Werle, B.O., "Sea Backscatter, Spikes and Wave Group Observations at Low Grazing Angles", IEEE International Radar Conference, pp. 187-195, 1995.
- 11. Stehwien, W., "Statistics and Correlation Properties of High Resolution X-band Sea Clutter", IEEE International Radar Conference, pp. 46-51, 1994.
- 12. Trizna, D.B., "Results of a Marine Radar Sea Clutter Experiments for Non-equilibrium Seas", IEEE International Radar Conference, pp. 192-196, 1989.
- 13. McLaughin, D.J., Allan, N., Twarog, E.M., Trizna, D.B., "High Resolution Polarimetric Radar Scattering Measurement of Low Grazing Angle Sea Clutter", IEEE Journal of Oceanic Engineering, Vol. 20, No 3, pp. 166-177, 1995.
- 14. Conte, E., Di Bisceglie M., Galdi, C., Ricci, G., "A Procedure for Measuring the Coherence Length of the Sea Texture", IEEE Trans. On Instrumentation and Measurements, Vol. 46, No 4, pp. 836-841, 1997.
- 15. Tonnerre, L., Muller, D., Maring-Leonard, C., Pinel. A., Waquet, A., "Comparative Statistical Analysis between Theoretical Model and Recorded Data for Sea Radar Return", Radar-97, IEE Conf. Proc. No 449, pp. 204-208, 1997.
- 16. Trizna, D.B., "Statistics of Low Grazing Angle Radar Sea Scatter for Moderate and Fully Developed Ocean Waves", IEEE Trans. On Antennas and Propagation, Vol. 39, No 12, pp. 1681-1690, 1991.
- 17. Farina, A., Gini, F., Greco, M.V., Verrazzani, L., "High Resolution Sea Clutter Data: Statistical Analysis of Recorded Live Data", IEE Proc.- Radar, Sonar, Navig., Vol. 144, No 3, pp. 121-130, 1997.
- 18. Corsini, G., Dalle Mese, E., De Palo, M., Mancianti, M., Ricci, A.M., Russo, F., Vanni, L., Verrazzani, L., "First Experimental Results Relevant to the

- Mediterranean Sea-Clutter", Proc. Of the 1989 International Symposium on Noise and Clutter Rejection in Radars and Imaging Sensors, IEICE, pp.37-41, 1989.
- 19. Antipov, I., "Analysis of Sea Clutter Data", DSTO-TR-0647, pp. 32, 1998.
- 20. Antipov, I., "Simulation of Sea Clutter Returns", DSTO-TR-0679, pp. 58, 1998.
- 21. Raghavan, R.S.,"A Method for Estimating Parameters of K-distributed Clutter", IEEE Trans, AES, Vol. 27, No 2, pp. 238-246, 1991.
- 22. Watts, S.,"Radar Detection Prediction in Sea Clutter Using the Compound K-distribution Model", IEE Proc., Vol. 132, Pt. F, No 2, pp. 613-620, 1985.
- 23. Watts, S.,"Radar Detection Prediction in Compound K-distributed Sea Clutter and Thermal Noise", IEEE Trans, AES, Vol. 23, No 1, pp. 40-45, 1987.
- 24. Farina, A., Russo, A., Studer, F.A., "Coherent Radar Detection in Log-Normal Clutter", IEE Proc., Vol. 133, Pt. F, No 1, pp. 39-54, 1986.
- 25. Schleher, D.C., "Radar Detection in Weibull Clutter", IEEE Trans, AES, Vol. 12, No 6, pp. 736-743, 1976.
- 26. Joughin, I.R., Percival, D.B., Winebrenner, D.P., "Maximum Likelihood Estimation of K-distribution Parameters for SAR data", IEEE Trans. Geosci. Remote Sensing, Vol. 31, pp. 989-999, 1993.
- 27. Walker, D., "Experimentally Motivated Model for Low Grazing Angle Radar Doppler Spectra of the Sea Surface", IEE Proc. Radar, Sonar Navig., Vol. 147, No 3, pp. 114-121, 2000.
- 28. Lee, P.H.Y. et al., "Power Spectral Lineshapes of Microwave Radiation Backscattered from Sea Surface at Small Grazing Angles", IEE Proc. Radar, Sonar Navig., Vol. 142, No 3, pp. 252-258, 1995.
- 29. Lee, P.H.Y. et al, "X-band Microwave Backscattering from Ocean Waves", Journal of Geophysical Research, Vol. 100, Pt. F, No C2, pp. 2591-2611, 1995.
- 30. Lee, P.H.Y. et al, "Lineshape Analysis of Breaking-wave Doppler Spectra", IEE Proc. Radar, Sonar Navig., Vol. 145, No 2, pp. 135-139, 1998.
- 31. Lee, P.H.Y. et al, "Wind-speed Dependence of Small-grazing-angle Microwave Backscatter from Sea Surfaces", IEEE Trans, AP, Vol. 44, No 3, pp. 333-340, 1996.
- 32. Frasier, S.J., Liu, Y., McIntosh, R., "Space-time Properties of Radar Sea Spikes and Their Relation to Wind and Wave Conditions", Journal of Geophysical Research, Vol. 103, No C9, pp. 18,745-18,757, 1998.
- 33. Jessup, A.T., Melville, W.K., Keller, W.C., "Breaking Waves Affecting Microwave Backscatter, 1. Detection and Verification", Journal of Geophysical Research, Vol. 96, No C11, pp. 20,561-20, 569, 1991.
- 34. Jessup, A.T., Melville, W.K., Keller, W.C., "Breaking Waves Affecting Microwave Backscatter, 2. Dependence on Wind and Wave Conditions", Journal of Geophysical Research, Vol. 96, No C11, pp. 20,547-20, 559, 1991.
- 35. Plant, W.J., Keller, W.C., "Evidence of Bragg Scattering in Microwave Doppler Spectra of Sea Return", Journal of Geophysical Research, Vol. 95, No C9, pp. 16,259-16,310, 1990.
- 36. Ward, K.D., Baker, C.J., Watts, S., "Maritime Surveillance Radar. Part 1: Radar Scattering from the Ocean Surface", IEE Proc., Vol. 137, Pt. F, No 2, pp. 51-62, 1990.
- 37. Allan, N., Trizna, D.B., McLaughin, D.J., "Numerical Comparison of Techniques for Estimating Doppler Velocity Time Series from Coherent Sea Surface Scattering Measurements", IEE Proc. Radar, Sonar Navig., Vol. 145, No 6, pp.367-373, 1998.

- 38. Posner, F.L., "Experimental Observations at Very Low Grazing Angles of High Range Resolution Microwave Backscatter from the Sea", NRL/MR/5310-98-8326, pp. 56, 1998.
- 39. Gorwols, B.L., Thompson, D.R., "Ocean Microwave Backscatter Distributions", Journal of Geophysical Research, Vol. 99, No C5, pp. 9741-9750, 1994.
- 40. Watts, S., Ward, K.D, "Spatial Correlation in K-distributed Sea Clutter", IEE Proc.-Pt.F, Vol. 134, No 6, October 1987, pp. 526-532.
- 41. Watts, S., "Cell-averaging CFAR Gain in Spatially Correlated K-distributed Clutter", IEE Proc.-Radar, Sonar, Navig., Vol. 143, No 5, October 1996, pp. 321-327
- 42. Raghavan, R.S., "A Model for Spatially Correlated Radar Clutter", IEEE Trans., AES, Vol. 27, No 2, pp. 268-275, 1991.
- 43. Baker, C.J., "Coherent and Polarization Properties of High Resolution Radar Sea Echo", Proc. of the 1989 International Symposium on Noise and Clutter Rejection in Radars and Imaging Sensors, pp.54-59, 1989
- 44. Baker, C.J., "K-distributed Coherent Sea Clutter", IEE Proc.-Pt.F, Vol. 138, No 2, April 1991, pp. 89-92.
- 45. Watts, S., Wicks, D., "Empirical Models for Detection Prediction in K-Distribution Sea Clutter", IEEE Radar Conference, 1990, pp. 189-194.
- 46. Di Bisceglia, M., Galdi, C. "Random Walk Based Characterisation of Radar Backscatter from the Sea Surface", IEE Proc. Radar, Sonar Navig., Vol. 145, No 4, pp. 252-258, 1998.
- 47. Boashash, B., (Ed.), "Time-frequency signal analysis. Methods and applications", Longman Cheshire, p. 547, 1992.
- 48. Davidson, G., Griffiths, H.D., Anderson, R., "Application of Multiscale Analysis to Coherent Pulsed Sea Clutter Returns", IEEE Radar Conference, 1999, pp. 300 -303.
- 49. Lee, P.H.Y. and others, "Scattering from Breaking Gravity Waves Without Wind", IEEE Trans, AP, Vol. 46, No 1, pp. 14-25, 1998.
- 50. Watts, S., "Radar Performance in K-distributed Sea Clutter", RTO SET Symposium on "Low Grazing Angle Clutter: Its Characterisation, Measurement and Application", RTO MP-60, pp. 372-379, April, 2000.

#### **DISTRIBUTION LIST**

## Statistical Analysis of Northern Australian Coastline Sea Clutter Data

#### Irina Antipov

#### **AUSTRALIA**

shared copy

#### **DEFENCE ORGANISATION**

Task Sponsor: DGAD

**S&T Program** 

Chief Defence Scientist

**FAS Science Policy** 

AS Science Corporate Management

Director General Science Policy Development

Counsellor Defence Science, London (Doc Data Sheet)

Counsellor Defence Science, Washington (Doc Data Sheet)

Scientific Adviser to MRDC Thailand (Doc Data Sheet)

Scientific Adviser Joint

Navy Scientific Adviser (Doc Data Sheet and distribution list only)

Scientific Adviser - Army (Doc Data Sheet and distribution list only)

Air Force Scientific Adviser

**Director Trials** 

## Aeronautical and Maritime Research Laboratory

Director

## **Electronics and Surveillance Research Laboratory**

Director (Doc Data Sheet and distribution list only)

Chief of Surveillance Systems Division: Dr. B. Ward

Research Leader Tactical Surveillance and Reconnaissance: Dr. J. Whitrow, SSD

Task Manager: B. Haywood, SSD

Author: I. Antipov, SSD

Dr. P.L. Choong, SSD

Mr. J. McCarthy, SSD

Mr. J. Baldwinson, SSD

### **DSTO Library and Archives**

Library Fishermans Bend (Doc Data Sheet)

Library Maribyrnong (Doc Data Sheet)

Library Salisbury

Australian Archives

Library, MOD, Pyrmont (Doc Data sheet only)

US Defense Technical Information Center, 2 copies

UK Defence Research Information Centre, 2 copies

Canada Defence Scientific Information Service, 1 copy NZ Defence Information Centre, 1 copy National Library of Australia, 1 copy

### **Capability Systems Staff**

Director General Maritime Development (Doc Data Sheet only)

#### **Knowledge Staff**

Director General Defence Knowledge Improvement Team (DGDKNIT) R1-3-A141, CANBERRA ACT 2600 (Doc Data Sheet only)

#### Army

Stuart Schnaars, ABCA Standardisation Officer, Tobruk Barracks, Puckapunyal, 3662(4 copies)

SO (Science), Deployable Joint Force Headquarters (DJFHQ) (L), MILPO Gallipoli Barracks, Enoggera QLD 4052 (Doc Data Sheet only)

#### Air Force

#### **P3C Project Office**

### Intelligence Program

DGSTA Defence Intelligence Organisation Manager, Information Centre, Defence Intelligence Organisation

## Corporate Support Program

Library Manager, DLS-Canberra

### UNIVERSITIES AND COLLEGES

Australian Defence Force Academy

Library

Head of Aerospace and Mechanical Engineering

Serials Section (M list), Deakin University Library, Geelong, 3217

Hargrave Library, Monash University (Doc Data Sheet only)

Librarian, Flinders University

#### OTHER ORGANISATIONS

NASA (Canberra)

AusInfo

State Library of South Australia

#### **OUTSIDE AUSTRALIA**

## ABSTRACTING AND INFORMATION ORGANISATIONS

Library, Chemical Abstracts Reference Service Engineering Societies Library, US Materials Information, Cambridge Scientific Abstracts, US Documents Librarian, The Center for Research Libraries, US

## INFORMATION EXCHANGE AGREEMENT PARTNERS

Acquisitions Unit, Science Reference and Information Service, UK Library - Exchange Desk, National Institute of Standards and Technology, US SPARES (5 copies)

Total number of copies:

48

Page classification: UNCLASSIFIED

DEFENCE SCIENC								
DOC	UME	NT CONTROL [	DATA		PRIVACY MARK DOCUMENT)	ing/c.	AVEAT (OF	
2. TITLE	3. SECURITY CLASSIFICATION (FOR UNCLASSIFIED REPORTS							
Statistical Analysis of Nor Data	THAT ARE LIMITED RELEASE USE (L) NEXT TO DOCUMENT CLASSIFICATION)							
Data	Document (U)							
	Title (U) Abstract (U)							
4.17.00.40				5 60	DDODATE AUTHOR		,	
4. AUTHOR(S)	5. CORPORATE AUTHOR Electronics and Surveillance Research Laboratory							
Irina Antipov	PO Box 1500 Edinburgh SA 5111 Australia							
6a. DSTO NUMBER		6b. AR NUMBER		6c. TYPE OF I	REPORT	7. DC	CUMENT DATE	
DSTO-TR-1236	l l			Technical Re	eport	November 2001		
8. FILE NUMBER	9. TASK NUMBER		10. TASK SPO	ONSOR	11. NO. OF PAGES		12. NO. OF REFERENCES	
9505/21/67/1		98/084	DGAD		84		50	
13. URL ON THE WORLDW	IDE WE	iВ		14. RELEASE AUTHORITY				
http://www.dsto.de	Chief, Surveillance Systems Division							
/DSTO-TR-1101.pdf	27 4 77 1	TO WE OF THE POOL						
15. SECONDARY RELEASE STATEMENT OF THIS DOCUMENT								
Approved for public release								
OVERSEAS ENQUIRIES OUTSIDE STATED LIMITATIONS SHOULD BE REFERRED THROUGH DOCUMENT EXCHANGE, PO BOX 1500, SALISBURY, SA 5108  16. DELIBERATE ANNOUNCEMENT								
16. DELIBERATE ANNOUN	CEIVIEIN							
No Limitations								
17. CASUAL ANNOUNCEM 18. DEFTEST DESCRIPTORS	1ENT		No limitations		-			
	1 0		26 : (1.0					
Sea clutter, Surveillance ra	idar, O	cean surveillance, P-	-3C aircraft, O	rion (reconnai	ssance aircraft)			
19. ABSTRACT	tho	results of detail	ad statistics	al analycic	of sea clutter da	ata th	at were collected	
This report describes the results of detailed statistical analysis of sea clutter data that were collected during the ESRL 38/97 trial, which was held off the Northern Australian coastline in February 1999. One								
of the trial's main objectives was to contribute to a database of experimentally collected clutter returns								
with radar system parameters that are comparable to those used in the Elta EL/M 2022A(V)3 maritime								
surveillance radar system Anti-Submarine Warfare mode. The validity of the compound K-distribution								
model has been proven for the collected sea clutter data both for amplitude and correlation properties.								

Page classification: UNCLASSIFIED